Transmitance Simulations for the Atmosphere with Clouds

Pecimotika, Mario

JOSIP JURAJ STROSSMAYER UNIVERSITY OF OSIJEK
DEPARTMENT OF PHYSICS

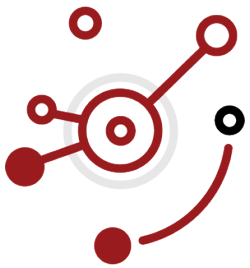

MARIO PECIMOTIKA

TRANSMITTANCE SIMULATIONS FOR THE ATMOSPHERE WITH CLOUDS

Master's Thesis

Osijek, 2018

JOSIP JURAJ STROSSMAYER UNIVERSITY OF OSIJEK
DEPARTMENT OF PHYSICS

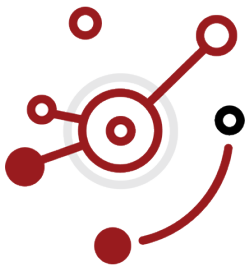

MARIO PECIMOTIKA

TRANSMITTANCE SIMULATIONS FOR THE ATMOSPHERE WITH CLOUDS

Master's Thesis
submitted to the Department of Physics,
Josip Juraj Strossmayer University of Osijek,
for the academic degree of
Master in Physics and Computer Science Education

Osijek, 2018

This thesis was made in Osijek under the supervision of Dr. Dario Hrupec, asst. prof., as a part of the Graduate Study in Physics and Computer Science at the Department of Physics, Josip Juraj Strossmayer University of Osijek.

J. J. Strossmayer University of Osijek
Department of Physics

Master's Thesis

TRANSMITTANCE SIMULATIONS FOR THE ATMOSPHERE WITH CLOUDS

Mario Pecimotika, B.Sc.

Abstract

A general requirement in ground-based γ-ray astronomy is a moonless night with good atmospheric transparency since the atmosphere is an integral part of every atmospheric Cherenkov telescope and its sensitivity considerably depends on variable atmospheric conditions. To fulfillment the above condition we need a clear atmosphere which is not always a case.

If clouds are present in the atmosphere, they have a considerable impact on the atmospheric transparency. However, from the HEGRA and MAGIC experiences, we know that sometimes is possible to operate the detector with considerably high efficiency in the presence of high dense cloud layers. Measurements of atmospheric transmission with MAGIC LIDAR at La Palma show that up to 30% of measurements made in conditions like those mentioned above can be used by applying proper corrections.

In this context, one of the aims of this thesis has been to study clouds impact on the atmospheric transparency, in order to show there is a possibility to prolongate duty cycle of CTA-N with observations during cloudy nights. In order to examine the influence of cloud altitude and optical depth on CTA-N performance, transmittance simulations for the atmosphere with clouds were made. The clouds simulations were done with MODTRAN computer program, while the atmospheric models produced by MODTRAN were used as inputs for Monte Carlo simulations with `sim_telarray`. Computed simulations can be used as a base for effective adaptive scheduling observations in the future.

(64 pages, 29 figures, 6 tables, 49 references)

Thesis deposited in Department of Physics library

Keywords: clouds, CTA-N, Monte Carlo methods, the atmosphere, transmittance

Supervisor: Dario Hrupec, Ph.D., Assistant Professor

Reviewers: Zvonko Glumac, Ph.D., asst. prof., Ivan Vazler, Ph.D., asst. prof.

Thesis accepted: 21st November 2018

Sveučilište J. J. Strossmayera u Osijeku
Odjel za fiziku

Diplomski rad

SIMULACIJE FAKTORA TRANSMISIJE ZA ATMOSFERU KOJA UKLJUČUJE OBLAKE

Mario Pecimotika, univ. bacc. phys.

Sažetak

Opći zahtjev u γ-astronomiji na površini Zemlje je noć bez mjesečine s dobrom atmosferskom transparentnošću. Atmosfera je sastavni dio svakog atmosferskog Čerenkovljevog teleskopa zbog čega njegova osjetljivost uvelike ovisi o promjenjivim atmosferskim uvjetima. Za ispunjavanje gore navedenih uvjeta trebamo čistu atmosferu, što nije uvijek slučaj.

Oblaci prisutni u atmosferi imaju nezanemariv utjecaj na atmosferksu transparetnost. Međutim, iz iskustva s teleskopima HEGRA i MAGIC znamo da je ponekad moguće, čak i u prisustvu slojeva oblaka velike gustoće, opažati s visokom učinkovitošću. Mjerenja faktora transmisije pomoću MAGIC LIDAR sustava na La Palmi pokazuju kako je moguće iskoristiti oko 30% mjerenja provedenih za vrijeme oblačnih noći primjenom podobnih korekcija.

U ovom kontekstu, jedan od ciljeva rada bio je proučiti utjecaj oblaka na atmosfersku transparentnost kako bi se pokazalo postojanje mogućnosti produljenja radnog ciklusa CTA-N, opažanjem tijekom oblačnih noći. Da bi se utvrdio utjecaj visine i optičke debljine oblaka na učinkovitost CTA-N, provedene su simulacije faktora transmisije za atmosferu s oblacima. Simulacije oblaka provedene su pomoću MODTRAN računalnog programa, dok su dobiveni atmosferski modeli korišteni kao ulazne datoteke za `sim_telarray` simulacije. Dobivene računalne simulacije mogu se koristiti u budućnosti kao polazište za učinkovito prilagodljivo planiranje opažanja.

(64 stranica, 29 slika, 6 tablica, 49 referenci)

Rad je pohranjen u knjižnici Odjela za fiziku

Ključne riječi: atmosfera, CTA-N, faktor transmisije, Monte Carlo simulacije, oblaci

Mentor: dr. sc. Dario Hrupec, docent

Ocjenjivači: doc. dr. sc. Zvonko Glumac, doc. dr. sc. Ivan Vazler

Rad prihvaćen: 21. studenog 2018.

Acknowledgements

Firstly, I would like to thank Dr. Dario Hrupec, asst. prof., my supervisor, whose guidance, direction and patience are especially appreciated. My sincerest thanks for your selfless help, your tireless work and constructive talks which have significantly contributed to my interest in the field of gamma-ray astronomy.

Many thanks to Dr. Dijana Dominis Prester, assoc. prof., and Dr. Saša Mićanović, asst. prof., from Department of Physics at the University of Rijeka for their hard work and for giving me the opportunity to include Monte Carlo simulations results in this thesis. I also owe thanks to Dr. Gernot Maier from the DESY accelerator center from Zeuthen, Germany, for the possibility of online access to the MODTRAN program.

Finally, I would like to thank my family, for their selfless support and love. For their patience over the past five years, for teaching me right from wrong and for encouraging me to keep my dreams in sight.

List of Figures

List of Tables

Preface

Cosmic rays are high-energy massive particles, mainly originating outside the Solar System and mostly from distant galaxies. Cosmic rays were discovered by Victor Hess at the beginning of 20th century. As observed at the top of the atmosphere, about 85% are protons, 12% are helium nuclei, 1% are heavier nuclei, whilst about 2% are electrons and positrons. Cosmic gamma rays are electromagnetic radiation of galactic and extragalactic origin. Cosmic rays with energies up to 10^{14} eV can be measured directly by balloon experiments or satellite detectors. Above tens of TeV, the flux of cosmic rays becomes insufficient for direct observations, but the atmosphere is used as a giant calorimeter for indirect ground-based observations.

Cherenkov telescopes are ground-based gamma-ray instruments used for the detection of very-high-energy gamma-ray photons in the photon energy range of 50 GeV to 50 TeV. An air shower is an extensive cascade of ionized particles or electromagnetic radiation produced in the atmosphere when a primary cosmic ray enters the atmosphere. If those secondary particles travel with speed greater than the speed of light in that medium, Cherenkov light is produced. Ground-based experiments are based on the detection of Cherenkov light. The most used are Imaging Atmospheric Cherenkov Telescopes (IACT).

The atmosphere is an integral part of Cherenkov imaging telescope, so the telescope response depends on the unpredictable atmospheric changes. Since there is no test-beam for Cherenkov telescope, Monte Carlo simulations are used instead. Monte Carlo simulations are usually made in two steps:

- simulation of particle showers in an atmosphere caused by the impact of cosmic rays (massive particles), cosmic gamma-rays or cosmic neutrinos, and
- detector simulations.

Cherenkov light can be attenuated in the atmosphere due to absorption and scattering. The ozone absorption is the dominant absorption process. Two scattering processes are important for Cherenkov light in the atmosphere: the Rayleigh scattering by molecules in the atmosphere and the Mie scattering, mainly by clouds.

The Cherenkov Telescope Array (CTA) is the next generation ground-based array of IACTs, the world's largest and most sensitive high-energy gamma-ray observatory, with more than 100 telescopes located in the northern (CTA-N) and southern hemispheres (CTA-S). The Observatorio del Roque de Los Muchachos (ORM) on the La Palma island, Spain is selected as a site for the northern array (CTA-N). Three classes of telescope will be distributed based on their sensitivity: the Small-Sized Telescope (SST), Medium-Sized Telescope (MST), and Large-Sized Telescope (LST). However, the CTA is no longer a distant future and nicely imagined project. On 20 October 2018, the inauguration of the prototype LST, named LST-1, on the northern site was held.

In order to examine the influence of cloud altitude and optical depth on CTA-N performance, transmittance simulations for the atmosphere with clouds were made. From previous experiences, e.g. with MAGIC telescopes, we know that is possible to prolongate telescope duty cycle if on measurements made during the cloudy weather, proper correction are applied. In order to determine the influence of clouds on the atmospheric transparency and performance of LST, we have done transmittance simulations and simulations of instrument response in such an atmosphere.

Cloud simulations are based on the following facts:

- low clouds remain almost always below the mountain peaks of La Palma and they are not included in the MC simulation,
- high cloud, cirrus, are thin and scattered, and mostly above the altitude at which the majority of Cerenkov photons is produced, and neither are them included in the MC simulations,
- altocumulus are scattered clouds, which is why particles shower can just pass through the cloud or miss it (such image will be distorted and treated as a cut off in the data analysis); the MC simulations for a uniform, 1 km thick altostratus are made. For ORM (placed at 2200 m), lower altostratus (below 3000 m) can be treated as a fog, and during foggy weather, observations are not performed anyway. Therefore, only the altostratus clouds with the base at 3000 m or more, are considered.

Transmittance simulation for the atmosphere with clouds were made with MODTRAN softver. Atmospheric models produced by MODTRAN were used as inputs for Monte Carlo simulations with `sim_telarray`. We suppose that clouds will have the greatest effects at low energies close to the threshold energy.

Contents

"We are made of the same stardust of which all things are made, and when we are immersed in suffering or when we are experiencing intense joy we are being nothing other than what we can't help but be: a part of our world."

— Carlo Rovelli, Seven Brief Lessons on Physics

Chapter 1

Very high energy gamma-rays

Electromagnetic radiation (EMR) is energy propagated through free space (vacuum) or a medium (e.g. vacuum, air, water etc.) in the form of electromagnetic waves. The very first prediction about the existence of electromagnetic waves was made by James Clerk Maxwell in 1864. Maxwell proposed in his electromagnetic theory that light is an electromagnetic disturbance in the form of waves [21]. In November 1886, Heinrich Hertz constructed the device that he named The Oscillator. At the ends of this device were two hollow zinc spheres connected to copper wires, while between the wires there was a gap. When Hertz applied a high voltage across that central gap, sparks were created. As Maxwell predicted, the oscillating electric charges produced electromagnetic waves (i.e. radio waves), which propagated through the air around the wires. That was the first experimental confirmation of Maxwell's electromagnetic theory [38].

Today is well established that time-varying electric fields can induce magnetic fields and vice versa. Because these fields generate each other, together they spread through a medium as transverse electromagnetic waves (i.e. EMR). Electric and magnetic fields in free space are always perpendicular to each other as well as to the direction of propagation (Figure 1.1). Electromagnetic waves in a vacuum always travel with the same speed, the speed of light:

$$c = 299\,292\,467\ \mathrm{ms}^{-1}.$$

EMR may be of *thermal* or *non-thermal* origin. Non-thermal radiation is due to cause other than the temperature of emitting body, i.e. when the characteristics of emitted radiation do not depend on the body's temperature (e.g., Compton scattering). Otherwise, we may discuss thermal radiation that depends on the temperature of energy source. Thermal sources have characteristic spectrum called the black-body radiation spectrum which is not a case for sources of non-thermal radiation.

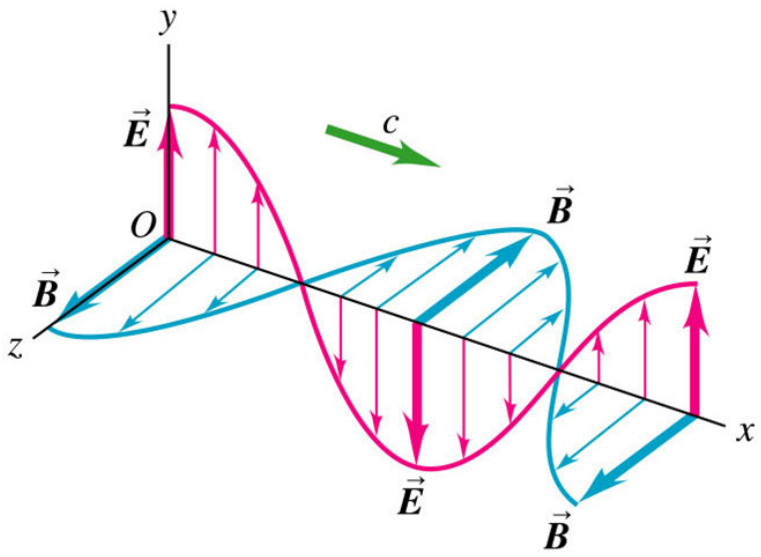

Figure 1.1: *Linearly polarizaed sinusoidal electromagnetic wave travelling in the positive x-direction.* [30]

EMR spans the huge range of frequencies f, i.e. wavelengths λ, where:

$$f = \frac{c}{\lambda}.$$

The electromagnetic spectrum is the distribution of electromagnetic radiation according to wavelengths, frequencies or energies. It covers all types of electromagnetic waves, ranging from wavelengths of several kilometers (such as radio waves) to less than 1 pm (such as gamma-rays) (Table 1.1).

Table 1.1: *Electromagnetic radiation spectrum.*

EMR			
Region	Wavelength (m)	Frequency (Hz)	Energy (eV)
Radio waves	> 0.1	$< 3{\cdot}10^{9}$	$< 0.1{\cdot}10^{-6}$
Microwaves	$0.1–1 \cdot 10^{-4}$	$3{\cdot}10^{9} – 3 \cdot 10^{12}$	$0.1{\cdot}10^{-6}$-$1{\cdot}10^{-3}$
Infrared	$1 \cdot 10^{-4} – 7.5 \cdot 10^{-7}$	$3 \cdot 10^{12} – 4.3 \cdot 10^{14}$	$1{\cdot}10^{-3}$-1
Visible	$7.5 \cdot 10^{-7} – 3.8 \cdot 10^{-7}$	$4.3 \cdot 10^{14} – 7.5 \cdot 10^{14}$	1-10
Ultraviolet	$3.8 \cdot 10^{-7} – 1 \cdot 10^{-9}$	$7.5 \cdot 10^{14} – 3 \cdot 10^{17}$	10-100
X-rays	$1 \cdot 10^{-9} – 1 \cdot 10^{-12}$	$3 \cdot 10^{17} – 3 \cdot 10^{19}$	100-100 000
γ-rays	$< 10^{-12}$	$> 3 \cdot 10^{19}$	$> 100\ 000$

A photon is the quantum of EMR. Photons with energies greater than about 100 keV are referred to as gamma-rays [18]. Since gamma-rays span over 16 orders of magnitudes in energy spectrum (10^4 eV $< E_\gamma < 10^{20}$ eV), there must be a large number of different techniques and instruments that enable more detailed study of gamma-rays. For that very reason, it is appropriate to classify gamma-rays in five different subregions depending on their energy (Table 1.2).

Table 1.2: *The gamma-ray energy subregions in the electromagnetic spectrum.*

Gamma-rays energy subregions	
Region	Energy
low energies (LE)	100 keV - 100 MeV
high energies (HE)	100 MeV - 100 GeV
very high energies (VHE)	100 GeV - 100 TeV
ultra high energies (UHE)	100 TeV - 100 PeV
extreme high energies (EHE)	> 100 PeV

Between 100 keV and 1 MeV, photoelectric absorption is the principal absorption mechanism. At higher energies (above 1 MeV) Compton scattering and electron-positron pair production becomes dominant. At these energies, gamma-ray satellite detectors are used. VHE gamma-rays phtons are produced in the acceleration of cosmic rays (CRs) or their interaction with the environment and typically are not detected by satellites because they simply pass through the detector. However, there is a solution to this problem as well. At the VHEs, gamma-rays are so energetic they can initiate electromagnetic cascades in the upper layers of the atmosphere (see Chapter 2). Cherenkov radiation (see Section 2.2) produced by these ultra-relativistic electrons and positrons can be detected by ground-based detectors [18].

Although gamma-rays cannot be directly detected by ground-based detectors (gamma-rays interact with the Earth's atmosphere, i.e. the atmosphere is non-transparent for gamma-rays), it is possible to detect VHE gamma-rays indirectly. VHE gamma-rays detection methods are presented in Chapter 2.

1.1 Gamma-rays production mechanisms

Gamma-rays can be produced by two different processes. In the first case, HE electrons or positrons can interact with magnetic and electric fields, where they produce, respectively, synchrotron and braking radiation. On the other hand, they

may also interact with LE photons via Inverse Compton scattering. The two preceding processes, induced by electrons and positrons, are said to be leptonic [9].

In the second case we can talk about decay (such as particle decay or radioactive decay) and annihilation (of pairs particle-antiparticle) processes. These processes involving nucleons and mesons are said to be hadronic [9].

Generally, all charged elementary particles may be sources of gamma radiation if accelerated in some way through external fields [40]. The above-mentioned gamma-rays production mechanisms are detailed described below.

1.1.1 Pion decay

Pions (π^+, π^-, π^0) are subatomic particles composed of one quark and one antiquark. They are the lightest of all mesons, and even more generally, of all hadrons. Pions are carrier of interaction between nucleons (they pull nucleons together). Since pions are unstable particles, they undergo to particle decay processes. As charged pions usually decay into muons and muon neutrinos, they are not as important as neutral pions that generally decay into gamma-rays (Figure 1.2). Neutral pion decays with a lifetime of $8.4 \cdot 10^{-17}$ seconds. There are the two most important π^0 decay modes. The primary decay mode of a π^0 , with a branching ratio[1] of 0.98823 is:

$$\pi^0 \rightarrow 2\gamma$$

and the second most common decay mode of a π^0, with a branching ratio of 0.01174 is:

$$\pi^0 \rightarrow \gamma + e^- + e^+.$$

Pions are produced in collisions between hadrons and in the processes when HE cosmic-ray protons and other hadronic cosmic-ray components interact with matter (i.e. atomic nucles) in the Earth's atmosphere. VHE gamma-rays can be produced by ultra-relativistic neutral pions. Since the pions are usually moving at a high velocity, the gamma-rays are emitted forward in a "V formation". This process gives a broad spectrum of gamma-ray energies.

1.1.2 Braking radiation

Braking radiation (bremsstrahlung) is an important loss mechanism for relativistic cosmic ray electrons and for the production of MeV photons (Figure 1.6). In

[1] Branching ratio is the fraction of particles which decay by an individual decay mode with respect to the total number of particles which decay.

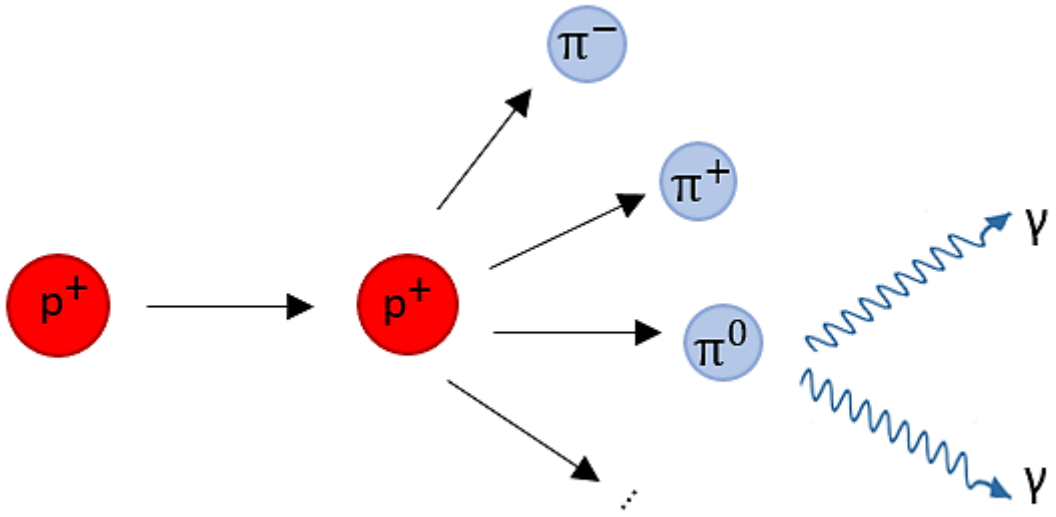

Figure 1.2: *Pion production and decay processes.*

the 1930s, Carl Anderson found that the ionisation loss rate given by the Bethe–Bloch formula (that describes the mean energy loss per distance travelled of swift charged traversing matter) underestimates the energy loss rate for relativistic electrons. The additional energy loss was associated with the EMR created by the acceleration of the electron in the electrostatic field of the nucleus called braking radiation or, in German, bremsstrahlung [18].

Braking radiation is emitted when charged particle is moving in an electric field at the expense of its kinetic energy. This mechanism is more efficient for the electrons than other charged particles (energy loss is far greater for low-mass particles [20]) and becomes dominant against the ionisation above critical energy at which the energy loss is equal for both ionisation and braking radiation [4]. Electrons can only emit gamma-rays if they have energy greater than $m_e c^2$. If the electron energy is lower, the energy loss by radiation will be negligible with regards to the energy loss by ionisation. The mean bremsstrahlung energy loss as a function of the distance traveled by the electron in the medium is given by:

$$-\frac{dE}{dx} = \frac{E}{\chi_0},$$

where χ_0 is the radiation length (the average distance over which the electron loses all but $1/e$ of its energy due to braking radiation) that depends on the density of the material and the atomic number Z:

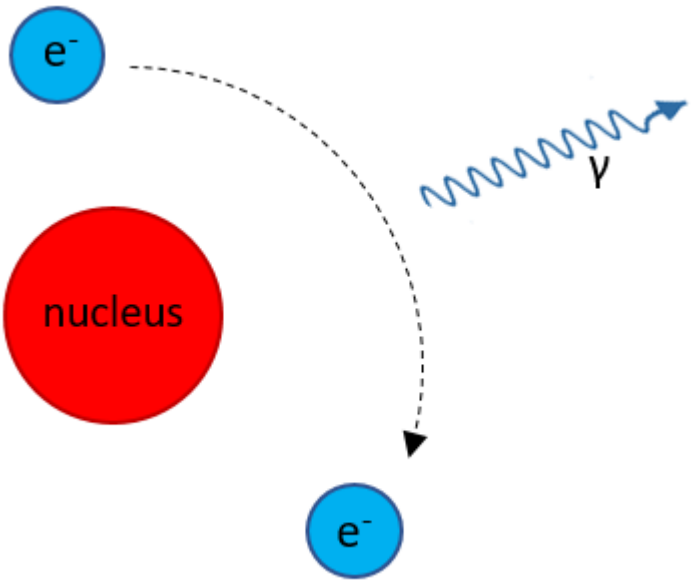

Figure 1.3: *Braking radiation*.

$$\frac{1}{\chi_0} = \frac{4Z^2N}{137} \cdot {r_0}^2 \ln\left(183 \cdot Z^{-\frac{1}{3}}\right),$$

where N is number of nuclei and r_0 electron radius [20]. Bremsstrahlung has a continuous spectrum which follows the same distribution as the charged particle. VHE gamma-rays photons can be produced by this mechanism only by UHE charges.

1.1.3 Synchrotron radiation

Synchrotron radiation (also known as magnetobremsstrahlung) is EMR emitted by the highly energetic charged particle that accelerates at the relativistic velocity in curved path or orbit due to magnetic field influence (Figure 1.7). This mechanism is more efficient in electrons than in protons. The synchrotron radiation does not normally reach VHE, however, it can work as target for other processes [4]. The intensity and frequency of the synchrotron radiation are directly related to the strength of the magnetic field and the energy of the charged particle (the higher the energy of the particles, the higher the intensity and the frequency of the emitted radiation). Synchrotron radiation does not depend on the temperature of a given astronomical source.

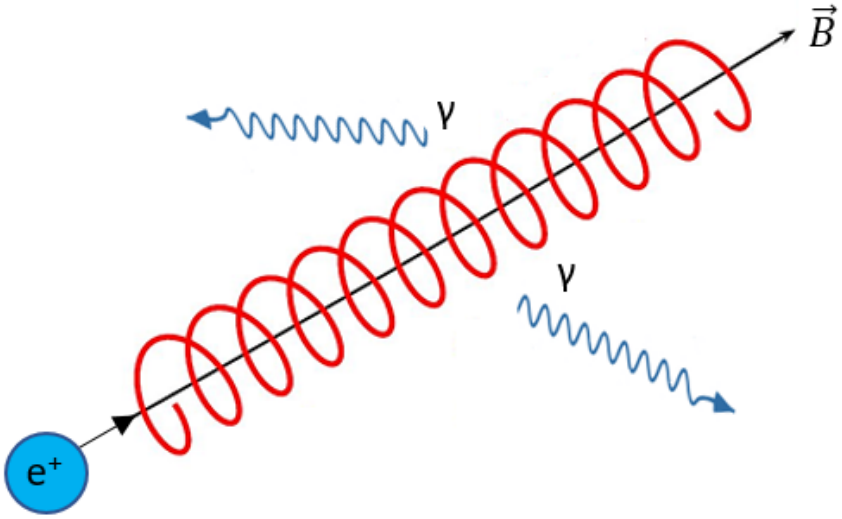

Figure 1.4: *Synchrotron radiation.*

1.1.4 Inverse Compton scattering

In inverse Compton (IC) scattering, LE photons are scattered by ultra-relativistic electrons. During the collision some of the electron's kinetic energy is transferred to the photon, resulting in wavelength decrease (Figure 1.5). If the electron's energy is high enough, this process can convert a radio photon into a gamma-ray photon. The low-energy photons may be the cosmic microwave background (CMB) radiation photons (the external IC) or the synchrotron photons emitted by the energetic electrons itself (synchrotron self-Compton) [14].

The energy transferred to the photon depends on the scattering angle at which the electron and photon meet. Minimum energy will be transferred when the scattering angle is 90°. For an example, the shock wave emerged in the SN explosion spreads the stellar material in the sourrounding area. Charged particles in the shock wave are accelerated practically to the speed of light. These ultra-relativistic electrons on their way may encounter LE photon (e.g. CMB photons) and transfer some of their energy to the photons, generating HE and VHE gamma-rays.

1.1.5 Particle-antiparticle annihilation

An annihilation occurs when a subatomic particle collides with its antiparticle, resulting in the production of two photons. That literally means both particle and antiparticle are disappeared. However, what remains is the energy contained in their

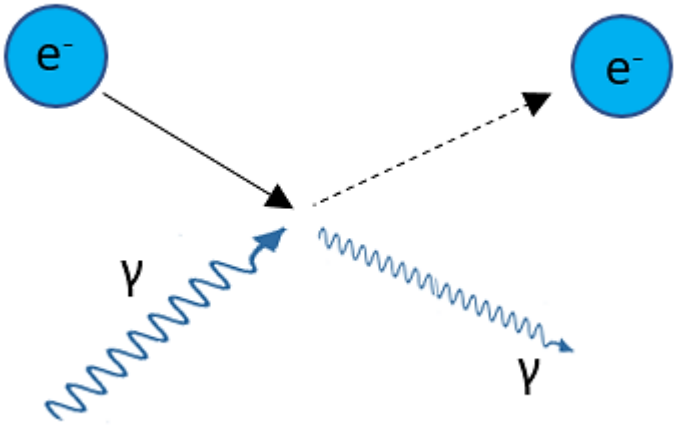

Figure 1.5: *Inverse Compton scattering.*

masses.

If the mass of the particle (antiparticle) was m, then the energy released by annihilation is at least equal to mc^2. This energy corresponds to the case of stationary particle and antiparticle. If particle and antiparticle were moving before the collision, their kinetic energies also play an important role - the energy remaining after the annihilation is equal to the sum of the two kinetic energies and the two rest energies.:

$$E_\gamma = 2mc^2 + E_+ + E_-,$$

where E_- and E_+ represent, respectively, the kinetic energy of the electron and positron. All processes must satisfy a number of conservation laws, such as conservation of electric charge, conservation of linear momentum and total energy, conservation of angular momentum and conservation of net lepton number.

For an example, electron-positron annihilation occurs when an electron and a positron collide (Figure 1.6). It is perhaps the most extreme form of energy loss mechanism for electrons. Positrons are usually produced by the decay of positively charged pions, π^+ or the radioactive decay of β^+ emitters [18]. Since the rest mass of an electron is equal to 0.51 MeV, each of two photons created by annihilation process must possess the same energy of 0.51 MeV:

$$e^- + e^+ \rightarrow 2\gamma.$$

Generally, electron and positron may interact without annihilation by elastic scattering. However, higher energies are required to create other heavier particles, such as D and B mesons, and W and Z bosons. The reverse mechanism, elec-

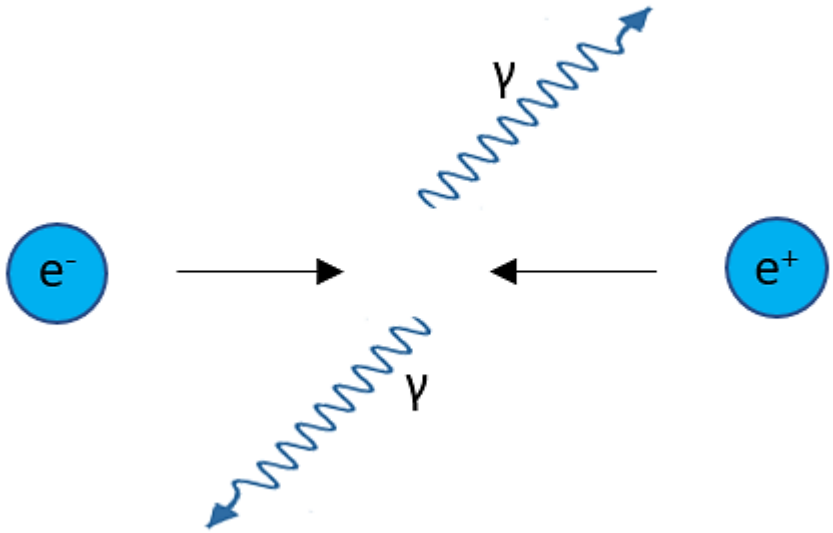

Figure 1.6: *Electron-positron annihilation.*

tron–positron creation, is a process of pair production.

1.2 VHE gamma-rays sources

The processes presented in Section 1.1 can occur in different astrophysical objects. A brief description of known VHE gamma-ray sources is presented below depending on their galactic or extragalactic nature [9].

1.2.1 Galactic sources

Supernova remnants A supernova (SN) is a transient, dramatic and catastrophic explosion that occurs during the last stadium of massive star's life. There are two types of SN explosions: SN I which releases typically 10^{51} erg[2] and there is no leftover in the core, and SN II which releases typically 10^{53} erg and the leftover in the core is a neutron star or a pulsar [14].

Supernova expels a huge amount of its material in the surrouding area at velocities up to 30 000 km/s what is 10% of the speed of light. A growing and expanding structure created after the SN explosion is called supernova remnant (SNR). SNR is actually a gaseous nebula that radiates in all regions of the electromagnetic spectrum: from radio waves to gamma-rays. There are also two types of SNRs with no hard

[2]Erg is a non-SI energy unit used in astrophysics. 1 erg = 10^{-7} J.

distinction: plerions and shell-type SNR. Plerions are young SNRs containing a pulsar and they are VHE gamma-ray sources (e.g. the Crab nebula and the Vela). Shell-type SNRs are HE gamma-ray sources.

In the best case scenario, SNR would be a uniform spherical shell because the energy realesed by the SN explosion wolud be distributed uniformly (equally in all directions). Shell-type remnants emit most of their radiation from a shell of expelled material. What we see is a brigth ring because there is more shocked material around the edges of the shell than in the other regions of the shell. Crab-type remnants (plerions) are the Crab Nebula-like SNRs. They are powered by a pulsar located at their center and they radiate from all regions of shell so there is no characteristic bright ring. Composite remnants are something between shell-like and Crab-like remnants, depending on what part of the electromagnetic spectrum is observed [34].

Radiation occurs because of the mutual collisions between expelled matter and with the surrounding interstellar matter (gas and dust). Since the rate at which the substance is expelled significantly exceeds the local speed of the sound, a powerful shock wave is formed. Simply put, SNRs are leftovers of the SN explosions. Gamma-ray are produced by the interaction between CRs, accelerated through the first order Fermi mechanism in the shock wave emerged in the SN explosion, and nuclei in the surrouding interstellar medium [4]. A model based on shock wave gives power law spectrum [14]:

$$\frac{dN}{dE} \propto E^{-2.7}.$$

Pulsars A pulsar is a highly magnetized and rapidly rotating neutron star (NS) usually 10 km in diameter and with unusually strong magnetic field of 10^8 T. The first pulsar was observed in 1967 by Jocelyn Bell. During the SN explosion, the core of a massive star is compressed and collapesd into a NS. After the explosion, NS retains most of its angular momentum. However, the NS's radius is considerably smaller than the radius of the former star, so the NS is formed with very high rotation speed to satisfy the law of conservation of momentum. A beam of radiation is emitted along the magnetic axis of the pulsar. The magnetic axis of the pulsar is not aligned with the rotational axis what causes the beam to be observed once in a every single period of the rotation of the NS - radiation is observed as pulses, much like the way the light from a lighthouse can be observed only when is pointed in the direction of the observer. It is strongly believed that pulsars have rotating magnetospheres, therefore, they potentially can drive charged particles (via second order Fermi acceleration) to high and ultra-high energies what could explain existence of UHECRs and EHCRs that exceed the GZK limit.

Binary systems and microquasars A binary system is a system of two astronomical object pulled together by their gravitational forces causes them to orbit each other around a barycenter. Microquasar is a binary system composed of a compact object, either a BH or NS, and a massive companinon star, e.g. red giant. The matter of the companion star is pulled by compact object forming an accretion disk around it. The system has two relativistic jets that generates strong radio waves, where perticles being accelerated and by inverse Compton interaction with the stellar wind VHE gamma rays are produced. Also, there is a presence of thermal radiation due to friction. The accretion disk becomes so hot and begins to emit X-rays so we can talk about X-ray binaries. However, both leptonic and hadronic processes are possible. The first microquasar SS433, was discovered in 1979 [14].

1.2.2 Extragalactic sources

Active galactic nuclei Active galactic nucleus (AGN) is an enormously energetic astrophysical object, a compact center of some galaxies, powered by an accretion of matter onto supermassive black hole (SMBH) (Figure 1.10). The radiation from AGN spans over more than twenty orders of magnitudes in frequency spectrum.

Today is a widely accepted idea that all AGNs are powered by SMBH located in their centers. AGN make up about 1% of all galaxies. A black hole (BH) is an extremely curved region of space-time that nothing, not even light, can escape from. Due to the conservation of angular momentum, the gas attracted by SMBH does not fall directly on it. Instead of that, an SMBH accretes surrounding material, which forms an accretion disk of hot plasma. Since the particles inside the disc are moving faster than the outer particles, their mutual collisions occur. In these turbulent processes, gravitational energy is transformed into thermal radiation. An accretion disk is surrounded by a dust torus that obscures a central SMBH and accretion disc and absorbs a huge amount of radiation. Thus, the heated dust torus also radiate, usually at infrared (IR) waveband.

Gamma-ray bursts Gamma-ray bursts (GRB) are sudden and extremely intense emissions of high-energy cosmic gamma-rays from the distant galaxies. These are the most luminous events in the universe. Their nature is still not completely clear, but two scenarios are the most probable: a hypernova (core-collapse supernova) or merger of two compact objects (e.g. neutron stars).

All GRBs can be divided into two groups: long and short. Long GRBs typically last 20 s and they have afterglow at lower energies: X, UV, optical, IR and radio. They originate from the supernova explosions. Short GRBs typically last 0.2 s, they have no afterglow and have much lower luminosity. They originate from the mergers of binary

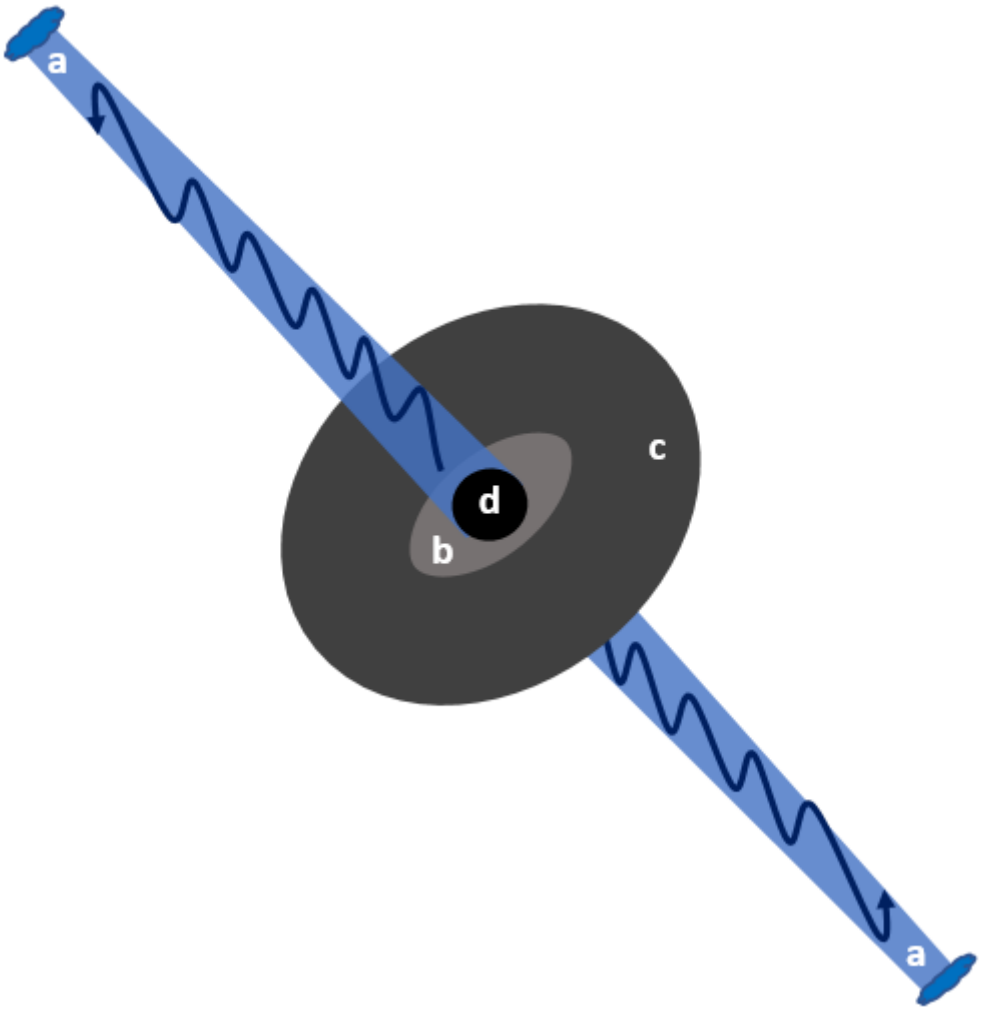

Figure 1.7: *Active galactic nucleus: a) relativistic jets (≈ 1 kpc), b) accretion disk (≈ 1 mpc), c) obsucring dust torus (≈ 1 pc), d) supermassive black hole. Note: Figure not drawn to scale.*

neutron stars (or a neutron star with a black hole).

Starburst galaxies Starburst galaxies are characterized by unusually high star-formation rates of order 10 – 100 $M_\odot$ per year [23]. The size of starburst regions is typically a few kiloparsecs in extent. It is supposed that the trigger of the star formation process is the tidal interaction of the galaxies passing next to each other or by their merger, resulting in the accumulation of substantial amounts of gas and dust in the central regions of the galaxy [34]. However, their lifespan is considerably short compared with the ordinary galaxies. Non-thermal radio synchrotron emission is detected from the hot plasma ejected from recent supernovae.

Chapter 2

Cherenkov light and gamma-ray detection techniques

Cosmic rays are HE massive particles, mainly originating outside the Solar System and mostly from distant galaxies. As observed at the top of the atmosphere, about 85% are protons, 12% are helium nuclei, 1% are heavier nuclei, whilst about 2% are electrons [18].

At the beginning of the 20th century, it was observed that charged electroscopes, after some time, spontaneously become neutral. At first it was supposed that the outbreak was the consequence of the ionization of air molecules due to radiation produced by the decay of radioisotopes present on the Earth. Soon it was proved that this ionization does not decrease with height increase, but, on the contrary, it slightly increases. Based on the ballon experiments performed by Victor F. Hess, a theory was established that this radiation comes from the universe, as it has been determined that it can not originate from the Sun (ionization did not change during the Sun's full eclipse in 1912) [9]. The term cosmic rays was proposed in 1925 by physicist Robert A. Millikan.

The CR spectrum (Figure 2.1) can be described by power law:

$$\frac{\mathrm{d}N}{\mathrm{d}E} \propto E^{-\alpha},$$

where α is the differential spectral index of the cosmic ray flux with values between 2.6 and 3.1, depending on the energy region [14][18][9]. The CR spectrum extends from approximately 10^8 to 10^{21} eV [4]. Up to about $4 \cdot 10^{15}$ eV the spectral index is equal to 2.7. The upper limit is called *knee* and it dependes on the carge: particles with higher charge will extend the knee to higher energies [4] [9]. The flux at this point reaches about 1 particle per m^2 per year. The spectral index above the knee rises about

3 and ends at region caleed *ankle* ($\approx 5 \cdot 10^{18}$ eV) [9]. The flux at this point reaches about 1 particle per km^2 per year. Finally, the spectrum changes again with the α about 2.6 (≈ 30 EeV). Particles with energies up to the knee are believed to be accelerated inside our galaxy, whilst particles above the ankle seem to have extragalactic origin [4][18]. Region between the knee and the ankle is still uncertain, but there are several proposals, such as the change in the acceleration mechanism or a cutoff of light elements, etc. Around the $\approx 5 \cdot 10^{19}$ eV should be a rapid change in α. The edge of CR spectrum is affected by the Greisen-Zatsepin-Kuzmin (GZK) cutoff. Traveling through the universe, CR particles lose their energy in collisions with low-energy photons such as the CMB photons. Einstein's special theory of relativity suggests that any CR that reaches the Earth from a source outside our galaxy will suffer so much collision on its way that its maximum energy would be only up to $\approx 5 \cdot 10^{19}$ eV, so-called GZK limit or cutoff:

$$p + \gamma_{CMB} \rightarrow p + \pi^0$$

$$p + \gamma_{CMB} \rightarrow n + \pi^0$$

Gamma rays are an integral part of the CRs. CRs with energies up to 10^{14} eV can be measured directly by balloon experiments or satellite detectors. Above tens of TeV the flux of cosmic rays becomes insufficient for direct observations, but the atmosphere is used as a giant calorimeter for indirect ground-based observations. Hence, measurement of higher energy CRs is performed indirectly by ground-based detectors. These detectors observe the secondary particles produced in the extended air showers (EASs).

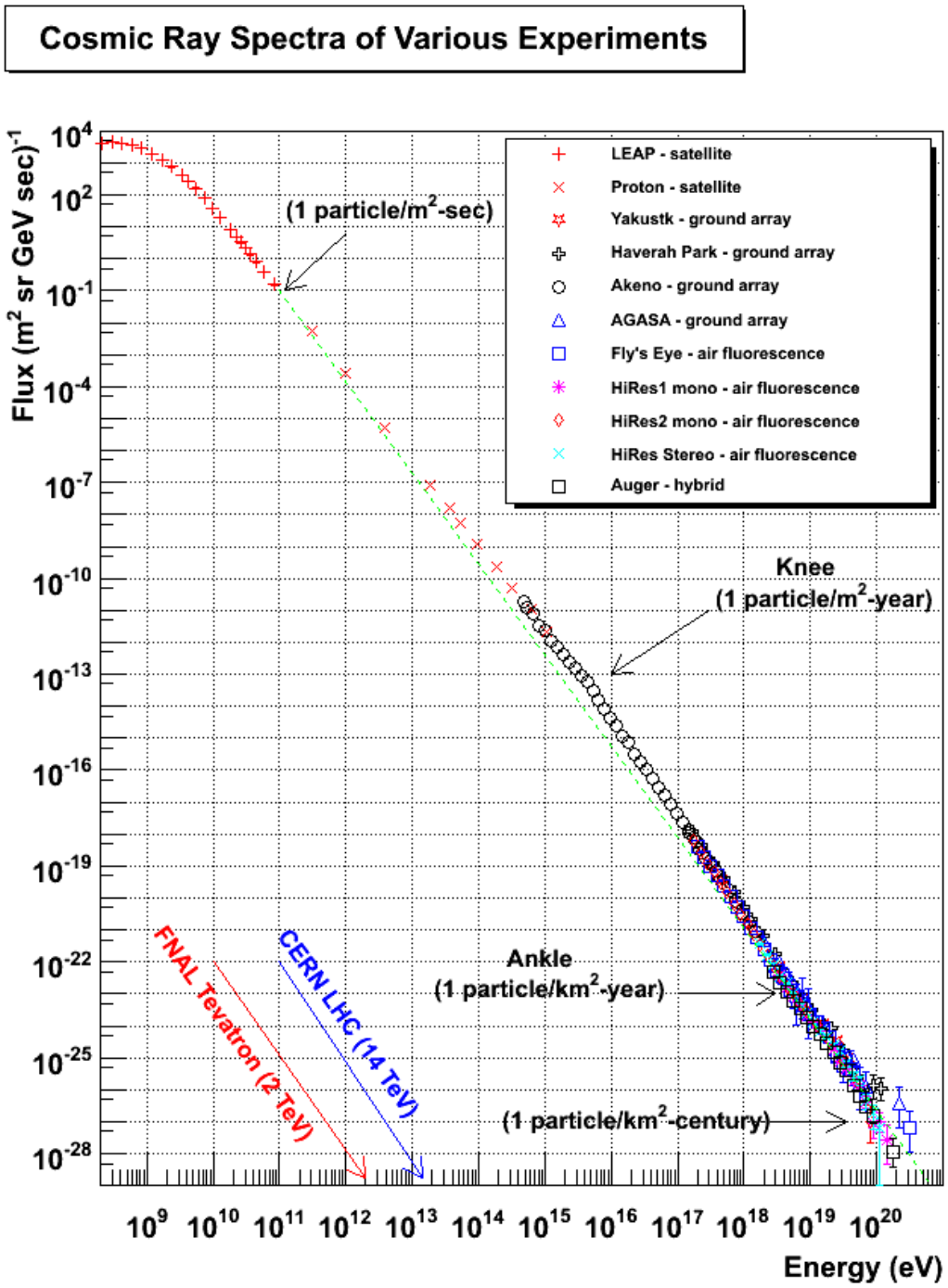

Figure 2.1: *CR spectrum of various experiments.* [37]

2.1 Extensive air showers

An air shower is an extensive cascade of ionized particles or EMR produced in the atmosphere when a primary cosmic ray enters the atmosphere [33]. The term *cascade* means that the incident particle collides with a nucleus present in the atmosphere producing a large number of energetic secondary particles. The term *extensive*

stands for many kilometers wide. They were first detected by Pierre Auger in 1938 and their studies led to important discoveries, such as the existence of the positron muons and pions [4]. There are two types of EASs: hadronic and electromagnetic showers (Figure 2.2).

Electromagnetic showers Gamma rays can initiate particle cascades through the electron-positron production or pion photoproduction process on nuclei present in the atmosphere if their energy is at least equal to 20 MeV [4]. Created electron-positron pair radiate gamma rays via bremsstrahlung in the electric field of nuclei. If photons emitted via bremsstrahlung have enough energy, they undergo pair creation as well, leading to a cascade. The process continues until the average energy of the particles reaches the critical value ≈ 86 MeV, below which the ionization energy loss dominates. In each step of the shower, the number of particles is doubled, while the particle energy decreases, until reaching critical value [4]. From this point the number of absorbed particles dominates over the number of created particles and the cascade diminishes. The characteristic amount of matter traversed for pair creation and bremsstrahlung is called the radiation length χ_0, wich is the mean distance over which a high-energy electron loses all but $1/e$ of its energy due to bremsstrahlung, but also a 7/9 of the mean free path for pair production by a HE photon [14][4]. The bremsstrahlung radiation length for electrons and positrons in the air is 37 g/cm^2. The "shower depth" is approximately determined by the relation:

$$\chi = \chi_0 \frac{\ln (E_0/E_c)}{\ln 2},$$

where $E_c = 800\text{MeV}/(Z + 1.2)$ is the critical energy (in the air ≈ 86 MeV) and E_0 is the initial energy. The depth of showers increases logarithmically with height, while the spreading of showers is mainly due to multiple electrons scattering [33][32].

Hadronic showers Hadronic showers are produced by the interaction between CRs particles, such as proton or nucleus, and nuclei present in the atmosphere. 90% of hadronic showers makes pions, but kaons, anti-protons, and nuclear fragments are also formed. The fragments of the incident nucleus and formed secondary particles travel through the atmosphere at high velocity until another nuclear reaction takes its place and so on. In the reactions, π^0 can be produced. Since neutral pions are unstable particles, they decay into two gammas, which in turn can initiate electromagnetic showers. We can distinguish three different components in the hadronic showers:

- **hadronic components** (π^0, π^+ and π^-, approximately in the same proportion, whilst ony neutral pions decay into two photons which can induce cascades),
- **electromagnetic components** (composed by secondary photons which mostly originate from the π^0 decay),
- **muonic components** (produced by the decay of charged pions).

Hadronic showers are wider (created pions can be emitted at wide angles to the incident CR direction, thus the transversal momentum of pions is higher than those in electrons and positrons). Also, in the hadronic showers there is a larger number of subshowers and, thus, greater asymmetry. However, the development of the electromagnetic showers is faster (it takes less than 3 ns to develop an electromagnetic cascade and up to the 10 ns to develop hadronic cascade) [4]. The radiation length for the initiating cosmic ray is ≈ 80 g/cm^2 while for gammas is ≈ 30 g/cm^2. Thus, hadronic showers develop deeper in the atmosphere.

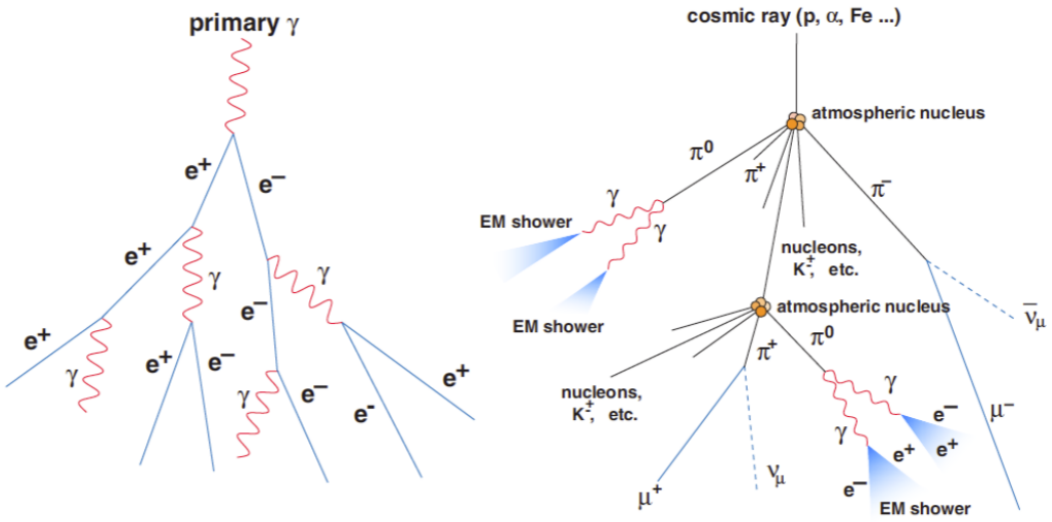

Figure 2.2: *Schemes of an electromagnetic (left) and hadronic (right) showers.* [4]

2.2 Cherenkov radiation

When an ultrarelativistic particle moves through a medium at a constant speed greater than the speed of light in that medium, it emits Cherenkov radiation. Cherenkov radiation has many applications, one of them in the detection of VHE gamma-rays. The HE gamma-ray can initiate electron-photon cascade and Cherenkov radiation can be emitted and detected by ground-based telescopes.

According to Maxwell's electromagnetic theory, an accelerating charged particle emits electromagnetic waves. However, in a quantum theory moving charged particle can excite molecules of the medium to the higher levels, i.e. excited states. Excited molecules can relax into ground state by emitting photons of a characteristic energy in the form of EMR. If the particle moves through a medium at a speed greater than the speed of light in that medium, the emitted waves add up constructively leading to a coherent radiation at angle θ with respect to the particle direction, known as Cherenkov radiation (Figure 2.3):

$$\cos\theta = \frac{1}{n\beta},$$

where $\beta = v/c$ and n is the refractive index of the medium, whose value varies with the wavelength of the Cherenkov light. Latter equation is known as Cherenkov relation and it flows a few important facts [14]:

- there is a threshold velocity $v_{min} = c/n$ below which no radiation takes place (the Cherenkov condition),
- for ultrarelativistic particle ($\beta \approx 1$), a maximum angle of emission is $\cos\theta_{max} = 1/n$,
- the radiation occurs mostly in the visible and near UV region ($n > 1$).

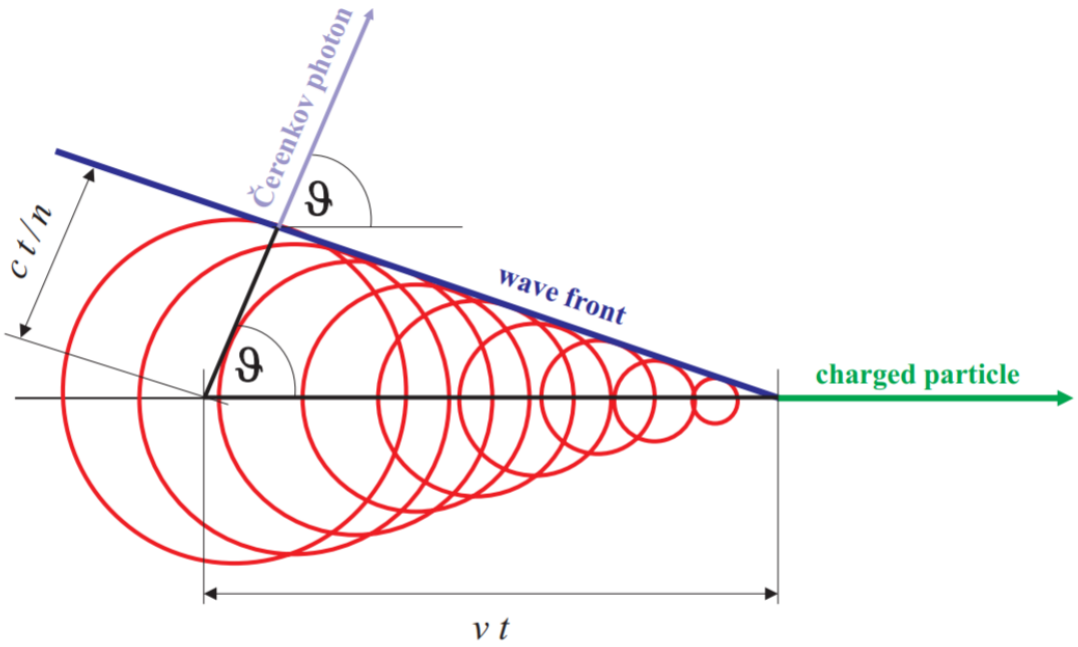

Figure 2.3: *Cherenkov radiation scheme.* [14]

The signature of the effect is a cone of emission in the direction of particle motion. Cherenkov radiation is only emitted if the particle has a velocity greater

than c/n. The mean value of θ in the air is ≈ 1 degree. Cherenkov photon's energy is proportional to the energy of the primary gamma-ray photon, therefore, this can be used to estimate the energy of the incident gamma-ray.

The Cherenkov radiation peaks in the UV band. There are some losses due to photons propagation through the atmosphere The main sources of this extinction are Rayleigh scattering (scattering off air molecules, with a strong wavelength dependency, affects mostly UV radiation), Mie scattering (scattering off aerosols, dust and water droplet, i.e. clouds, does not show any strong wavelength dependency) and ozone molecules (responsible for the strong absorption of photons with energies less than 300 nm) [4]. There is also a dependency on the zenith angle (ZA) of EAS. At high ZA, cascades are developed in the highest layers of the atomsphere and they travel a larger path. Obviously, the higher the ZA, the higher the extinction [4]. Extinction (attenuation) of Cherenkov light in the atmosphere is detailed in Chapter 4.

Frank-Tamm formula can be used to calculate the total amount of energy emitted per unit path:

$$\frac{\mathrm{d}E}{\mathrm{d}l} = \left(\frac{e}{c}\right)^2 \int \left(1 - \frac{1}{\beta^2 n(f)^2}\right) f \,\mathrm{d}f,$$

where n is an index of refraction of the medium which is frequency (wavelength) dependent [14].

The Cherenkov light distribution produced by electromagnetic showers differs from that of hadronic showers. Cherenkov light retains the original direction of the incident photon. The Cherenkov image of an EAS produced by a gamma-ray points toward the center of the camera since the axis of the EAS is orientated parallel to the optic axis of the telescope. However, hadronic showers arrive randomly distributed, resulting EAS images point in all directions in the camera.

2.3 Gamma-ray detection techniques

There are two types of gamma-ray detection techniques: space-based gamma-ray observatories and ground-based gamma-ray observatories. Gamma-rays with energies above ≈ 1 TeV cannot be detected directly because the collection areas of satellites are too small for the very low flux of highly energetic radiation. Ground-based detectors can overcome this problem but gamma-rays can only be detected indirectly because incident gamma-ray photons collide and interact with the Earth's atmosphere, so ground-based detection relies on the EAS production.

Space-based experiments provide information from 1 MeV to a few hundred

GeV (they have wide Field of View[1] (FoV), excellent γ/hadron separation, poor angular resolution[2] at low energies, but very good energy resolution with small systematic errors) [4].

Ground-based experiments are based on the detection of Cherenkov light (Imaging Atmospheric Cherenkov Telescopes (IACTs) and Water Cherenkov arrays). IACTs have very big collection areas, they provide very good γ/hadron separation and excellent angular resolution. However, daytime observations are not possible. Water Cherenkov arrays have very large collection area, full duty cycle (daytime observations are possible) and very wide FoV. However, γ/hadron separation and angular resolution are poor [4]. While IACT detect the Cherenkov light of the shower particles in the atmosphere, Water Cherenkov detectors detect the Cherenkov light in the detector, i.e. the water.

In this thesis, I will briefly describe some currently operating space-based and ground-based experiments. In next section, a detailed description of future Cherenkov Telescope Array (CTA) will be given.

INTErnational Gamma-Ray Astrophysics Laboratory (INTEGRAL) INTEGRAL is a currently operational space-based telescope for observing gamma-rays. INTEGRAL consists of four instruments: a gamma-ray spectrometer (SPI, the SPectrometer for INTEGRAL) (20 keV 8 MeV), an imager (IBIS, Imager on-Board the INTEGRAL Satellite) observes from 15 keV (hard X-rays) to 10 MeV (gamma rays) with angular resolution of 12 arcmin, an X-ray monitor (3 eV 35 keV) and an optical monitor (OMC, INTEGRAL mounts an Optical Monitor), allowing simultaneous observations of a source in the visible, X-ray and gamma-ray bands. It was designed to study celestial gamma-ray sources in the 15 keV to 10 MeV energy range, BHs, NSs, SNs, AGNs, and GRBs. It was launched on October 17 2002 [48][44].

The Fermi Gamma-ray Space Telescope (FGST) FGST, formerly called the Gamma-ray Large Area Space Telescope (GLAST), is a currently operational space-based telescope for gamma-ray astronomy observations from low Earth orbit. It is used to study AGNs, pulsars and other HE sources and dark matter. Its main instruments are the Large Area Telescope (LAT) and the Gamma-ray Burst Monitor (GBM). Fermi was launched on 11 June 2008 [47].

[1] Field of View (FoV) is a solid angle through which a detector is sensitive to electromagnetic radiation.

[2] The angular resolving power (or resolution) of a telescope is the smallest angle between close objects that can be seen clearly to be separate.

Imaging Atmospheric Cherenkov Telescope (IACT) IACT is the type of VHE gamma-ray detectors. As I previously said, VHE gamma-ray interacts with atoms and molecules present in the atmosphere, producing EASs. Ultrarelativistic electrons and positrons generate Cherenkov radiation. The Cherenkov light flash lasts few nanoseconds. The intensity of Cherenkov photon is proportional to the energy of incident gamma-ray. Detection of cosmic charged particles cannot give the identification of their source because magnetic fields divert particles' trajectory. However, magnetic fields do not affect gamma-rays and we are able to identify the source of the incident cosmic gamma ray. Hence, Cherenkov's photons are seen in the telescope camera as an image whose characteristics allow the identification of the incident gamma-ray and the determination of its initial direction and energy.

Due to the change of the atmospheric density with altitude (and therefore, the refractive index of air), the Cherenkov angle increases from 0.2° at an altitude of 30 km to 1.5° at sea level [24]. An ultrarelativistic particle propagating vertically through the atmosphere produces Cherenkov light projected to the ground. The contribution of all particles involved in the EAS that emit Cherenkov radiation leads to a full circle on the ground, forming the Cherenkov light pool, typically 120 m in diameter (Figure 2.4) [4]. All the information we can use is deposited in the shape and the intensity of the light pool captured by the Cherenkov telescopes.

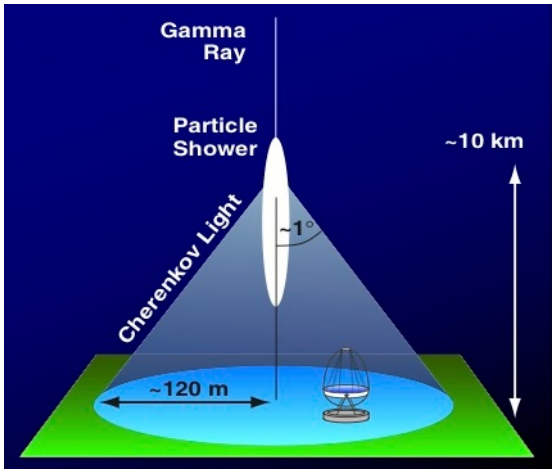

Figure 2.4: *Cherenkov light pool.* [43]

The CCD cameras have the time accuracy of approximately 1 ms and they are useless for Cherenkov light detection. A way to capture these very shorts flashes is by using PMTs (photomultiplier tubes) [24]. The size of each PMT determines the angular resolution of the telescope, while the number of PMTs determines the FoV. Both high sensitivity and good time resolution are required as the Cherenkov pulses are extremely short and weak.

The goal is to link every light pool with every single event. It is possible to identify three different regions of a single event [24]:

- **the head** is the region of the shower between the first interaction and the point where the particles produced are half of the maximum number of particles produced in all the shower,
- **the core** that includes the region with the maximum number of particle produced,
- **the tail** is the region where the number of secondary particles increases.

High Energy Stereoscopic System (H.E.S.S.) H.E.S.S. is a type of IACT for the investigation of cosmic gamma rays in the photon energy range of 0.03 to 100 TeV named after Victor F. Hess. H.E.S.S. is located 1.8 km above sea level (asl) in the Khomas Highlands of Namibia, Africa, it has been operating since June 2002 and consists of four 12 m-diameter IACTs arranged in a square of side 120 m, and one 28 m-diameter IACT placed in the centre of the array [46].

Very Energetic Radiation Imaging Telescope Array System (VERITAS) VERITAS is an IACT with an array of four 12 meter optical reflectors for gamma-ray astronomy in the GeV - TeV regime with an approximate separation of 100 meters, placed at Mount Hopkins, Arizona, USA. It studies SNRs, pulsars, AGNs, dark matter, GRBS, unidentified sources of CRs etc. The full array has been operational since January 1, 2007 [45].

Major Atmospheric Gamma Imaging Cherenkov Telescopes (MAGIC) MAGIC is a system of 2 IACTs of 17 m diameter (Figure 2.3). The MAGIC collaboration involves 12 countries: Armenia, Brasil, Bulgaria, Croatia, Finland, Germany, India, Italy, Japan, Poland, Spain, Switzerland. It is located at the Roque de Los Muchachos in the North-Atlantic Canary island of La Palma (2200 m asl, 28.8 °N, 17.8 °W) [24]. This location was chosen because of optimal observational conditions (the relative humidity is usually below 10% and cloudy days make less than 15% of days throughout the year).

In 2004, the first telescope, MAGIC I, was installed as a monoscopic system with an integral flux sensitivity around 1.6% of the Crab flux for a peak energy of 280 GeV in 50 hours of observation [3]. In 2009, the second telescope, MAGIC II, at a distance of 85 m from the first one, started taking data. Together they integrate the MAGIC telescope stereoscopic system with sensitivity improved up to $0.76 \pm 0.03\%$ of the Crab Nebula flux for energies greater than 290 GeV in 50 hours of observations [4]. After 2011-2012 major upgrade, an integral sensitivity of $0.66 \pm 0.03\%$ of the Crab Nebula flux in 50 hours above 220 GeV was achieved [4].

The supporting structure of the telescope consists of light carbon fiber-epoxy tubes. The total weight of the structure, including the reflector and the camera support, is less than 20 tons what allows a fast repositioning of the telescopes. Telescopes are moved on a 20 m diameter circular rail by two 11 kW motor, one along the azimuth angle (-90° to 318°) and the other one along the zenith angle (-70° to 105°) [4] [24]. For any orientation, the deformation of the structure is lower than 3.5 mm [4]. The reflector is made of aluminum panels arranged to form a parabolic surface what guarantees the best isochronous response of the mirrors [24] with the focal ratio $f/D = 1$. This is important in large-sizeed detectors because the arrival timing difference of the reflected light from different parts of the dish becomes also larger [4].

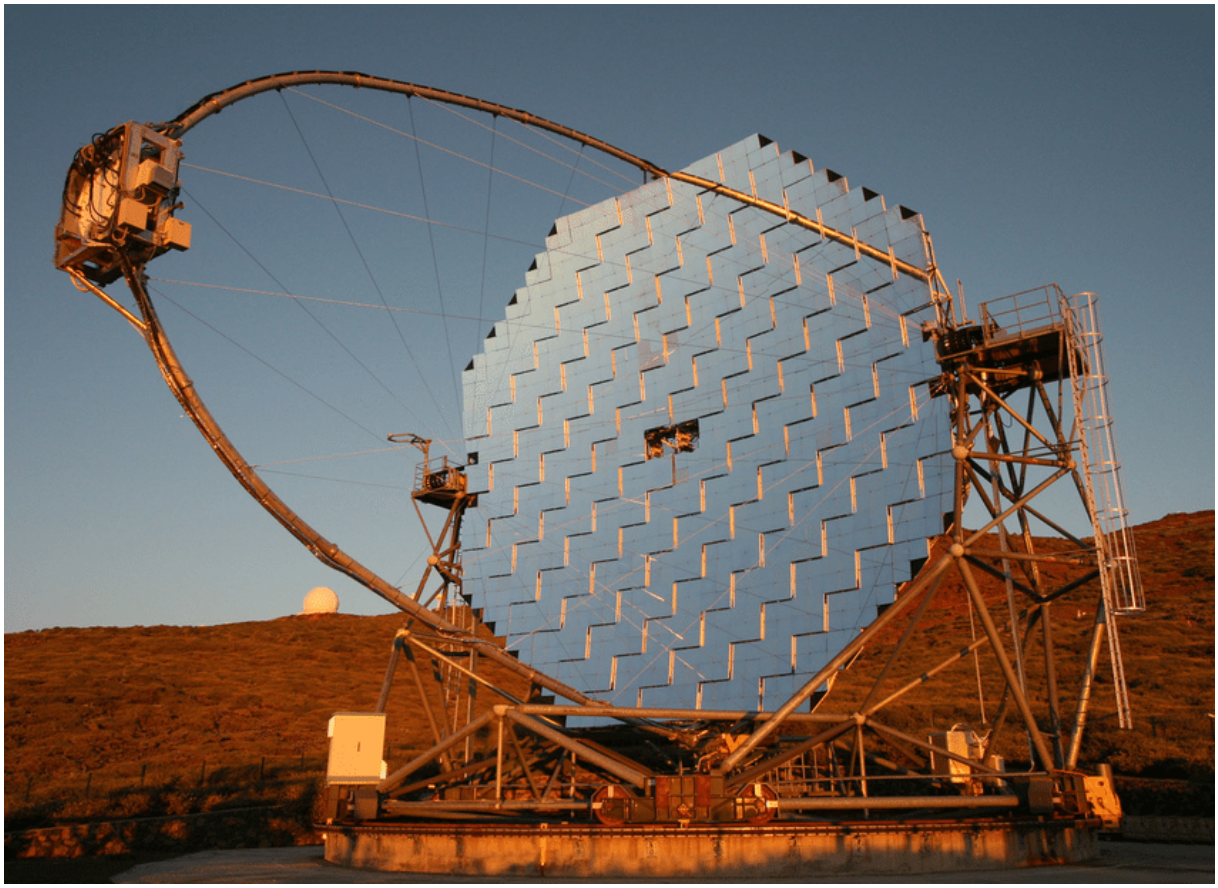

Figure 2.5: *One of the 17 m diameter MAGIC telescopes located on the Canary Island of La Palma.* [29]

Both MAGIC I and MAGIC II cameras present circular shape with ≈ 1.2 m diameter and a FoV of 3.5°. The MAGIC I telescope camera was made of 577 PMTs. The PMT tubes form a hexagonal structure thanks to which the camera is covered with minimal blind surfaces. Tubes are coated with WLS (Wave Length Shifter) material to take advantage of UV wavelength of Cherry Light, and improved quantum efficiency.

The telescoping camera consists of an 397 inner pixels 25 mm diameter, outer 180 pixels 39 mm diameter and 18 pixels for testing. Quantum efficiency the camera is about 25%. The MAGIC II camera consists of 1183 pixels grouped in a hexagonal 7-pixel structure, forming a cluster that can be easily replaced. Pixels are also made of PMTs. The camera has a total of 169 clusters of which 92 central clusters make the trigger area, covering FoV of 2.5°.

Triggers are used to decide whether a particular event will be accepted and later analyzed or not, i.e. to distinguish the gamma-ray induced cascades from the background night sky [4]. Level 0 trigger (L0T) it is the ground-state discrimination level for each PMTs. Level 1 trigger (L1T) it is the next-neighbor time-coincidence check (checks whether are the signals that passed the L0T from 2, 3, or 4 adjacent pixels or not). Level 2 trigger (L2T) it is the topological discrimination level (it is used for events discrimination based on the angular rotation of the image created in the detector). Level 3 trigger (L3T) it is the stereo trigger level (it is used to ensure that both telescopes actually recorded the same Chenrekov light) [24].

2.4 Cherenkov Telescope Array

The Cherenkov Telescope Array or CTA is a multinational, worldwide project to build a new generation IACTs at the northern hemisphere (CTA-North, CTA-N) which will study extragalactic sources at the lowest possible energies, and a second array at the southern hemisphere (CTA-South, CTA-S), which will concentrate on galactic and cover the full energy range sources. The CTA will perform measurements in the VHE range, between several tens of GeVs up to several hundred TeVs. The project currently makes 1200 scientists and engineers working in 200 different institutions in 32 countries around the world. In June 2015, the sites were choosen: the Observatorio del Roque de Los Muchachos on the La Palma island, Spain for the northern array (CTA-N), and a site close to Paranal Observatory, Chile for the southern array (CTA-S) [2]. CTA will observe the following key targets: galactic centre, Large Magellanic cloud, galactic plane, galaxy clusters, cosmic Ray PeVatrons, AGNs, GRBs [28].

Currently operating IACTs are sensitive in an energy range of 80 GeV - 50 TeV, have a typical FoV of 3°-5°, their angular resolution is currently around 1 arcmin above 1 TeV and their energy resolution approaches 10% well above the threshold. Extending the observations below 80 GeV is crucial for studies of galactic sources and below 80 GeV to understand acceleration mechanisms in galactic objects like SNRs. Lowering the energy threshold is crucial for the observation of distant extragalactic sources whose gamma-rays comes with a low flux due to interaction with extragalactic

background light. Larger FoV will allow for a full VHE sky survey and a sub-minute time resolution will allow detailed observations of sources like GRBs and AGNs [2].

The CTA design has been developed on few basic ideas: increase the array size up to ≈ 100 telescopes, distribute telescopes over a large area (110 km^2), make use of telescopes of at least three different sizes and increase automation and remote operation [2]. A large number of telescopes will allow for independent operation of subarrays, with the sensitivity of current telescopes or better, pointed to observe one source or to cover a large area of the sky. The CTA concept was first proposed in 2006 with an estimated investment cost of around 150 million euros [1]. CTA can reach angular resolutions of better than 2 arc minutes for energies above 1 TeV, a factor of 5 better than the typical values for current instruments [1]. To reach the presented performance goals and the wide energy range, the instrumentation will be adjusted in three energy ranges: the low-energy range ≤ 100 GeV, the core energy range 0.1–10 TeV, the high-energy range > 10 TeV [28].

2.4.1 CTA telescopes

Three classes of telescope will be distributed based on their sensitivity: the Small-Sized Telescope (SST), Medium-Sized Telescope (MST), and Large-Sized Telescope (LST) (Table 2.1, Figure 2.6, Figure 2.7). SSTs are tuned to be the most sensitive and they are ideal for the southern array and detection of gamma-rays of higher energies. MST and LSTs will be installed on both the southern and the northern location [28].

Table 2.1: *Site characteristics for the CTA Paranal (CTA-S) and La Palma sites (CTA-N).* [19]

Site	Longitude, Latitude	Altitude	LSTs	MSTs	STSs
Paranal	70.3° W, 24.07° S	2150 m	4	25	70
La Palma	17.89° W, 28.76° N	2180 m	4	15	0

Large-Sized Telescope (LST) Four (both in the southern and northern hemisphere array) LSTs will be arranged to cover the energy between 20 and 150 GeV with very good sensitivity up to energies of several TeVs. The LST is an alt-azimuth telescope with a 23 m diameter parabolic mirror of a reflective surface of 370 m^2 and the focal length of 28 m. LST will be 45 m tall and weigh around 100 tonnes, but extremely agile (the goal is to achieve the re-position within 20 seconds). Some other specifications are: 4.3° FoV, pointing precision less than 14 arcseconds, $f/d = 1.2$. On Wednesday, 10

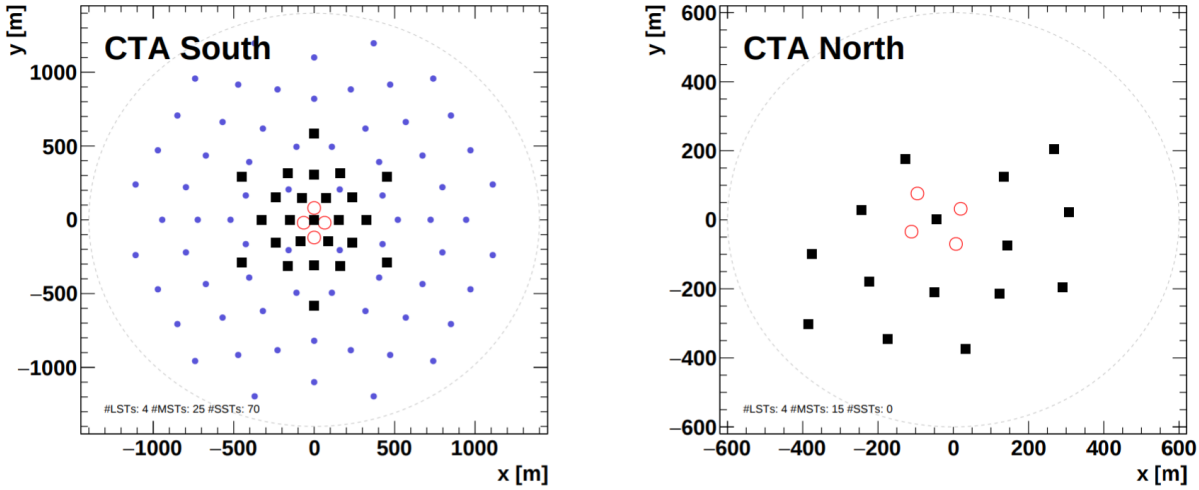

Figure 2.6: *Telescope layouts for the CTA-S (left) and CTA-N (right). The open circles indicate LSTs, the filled squares MSTs, and the filled points STSs.* [19]

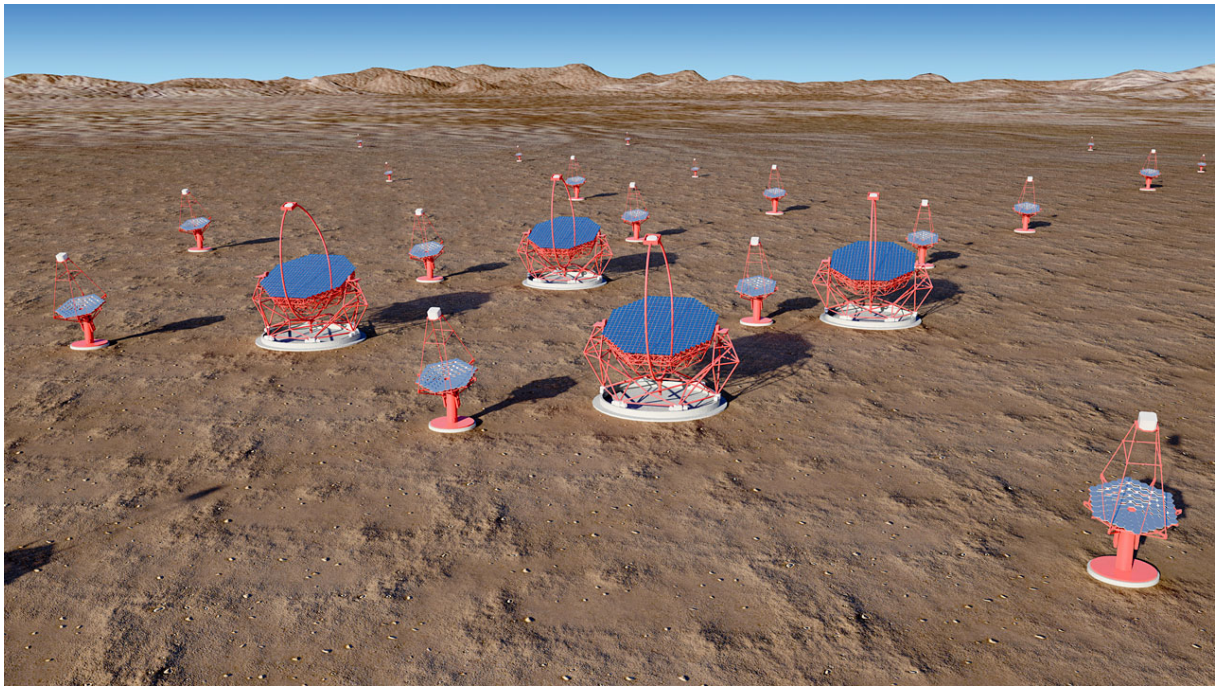

Figure 2.7: *CTA telescopes.* [27]

October 2018, the inauguration of the prototype LST, named LST-1, on the northern site was held. The Cherenkov camera has 1855 pixels divided into 265 PMT modules with a peak quantum efficiency of 42%. The camera trigger strategy is based on the shower topology and the temporal evolution of the Cherenkov signal produced in the camera [28] [2].

Medium-Sized Telescops (MST) The Medium-Sized Telescope (MST) will have sensitivity in the core energy range (between 150 GeV and 5 TeV). There will be 40 MSTS (25 in the southern hemisphere and 15 in the northern hemisphere). The MST is a telescope with an 11.5 m diameter parabolic mirror of a reflective surface of 88 m^2 and the focal length of 16 m. The goal is to achieve the re-position within 90 seconds. Some other specifications are: pointing precision less than 7 arcseconds, $f/d = 1.3$, FoV $\approx 8^o$. The MST mirror will have two different camera designs that use PMTs with a FoV of about 8^o (NectarCAM with 265 modules and FlashCAM with 12 PMTs arranged in a hexagonal structure) [28] [2].

Small-Sized Telescope (SST) There will be 70 Small-Sized Telescopes (SSTs) spread out over several square kilometers in the southern hemisphere array only with the sensitivity between a few TeV and 300 TeV. Three different SST implementations are being prototyped and tested: one single-mirror design (SST-1M) and two dual-mirror designs (SST-2M ASTRI and SST-2M GCT). The current expectation is that the array will include a mixture of these designs. The SST will have a 4 m diameter mirror with large FoV of about 8^o-10^o. Positioning time will be less than 60 seconds with the pointing precision of less than 7 arcseconds.

The SST-2M ASTRI will have 4.3 m diameter primary mirror and the 1.8 m secondary mirror, with the focal length 2.15 m. There will be 2368 pixels in Cherenkov camera with the FoV of 10.5^o. The SST-1M will have 4 m diameter mirror with the focal length 5.6 m and will use an innovative camera based on silicon photomultipliers (SiPMs) that can operate during high levels of moonlight. A camera will consist of 195 pixels with the FoV of 8.8^o. The SST-2M GCT will have 4 m diameter primary and 2 m secondary mirrors. Camera will have 2048 pixels and the FoV of 8.3^o [28] [2].

2.4.2 CTA performance

The sensitivity at energies below 200 GeV will be very similar for both CTA arrays, with high sensitivity down to energy of $\approx$ 20 GeV (Figure 2.8). The achieved sensitivity reaches 0.2% of the flux of the Crab Nebula at 200 Gev - few TeV range, roughly one decade better than curently operation IACTs. At the highest energies, the effect of night sky background (NSB) approaches zero.

Typical values for the energy resolution are 5-10% (Figure 2.9). Typical values for the angular resolution are 0.1^o at 100 GeV and 0.02^o-0.03^o above 1 TeV (Figure 2.10). The LSTs will be of highest sensitivity in the range 20 GeV - 200 GeV, 100 GeV to 5 TeV for the MSTs, and the highest energies for the SSTs. The large FoV of up to 8 degrees for MSTs and SSTs results in a relatively small decrease of sensitivity as a

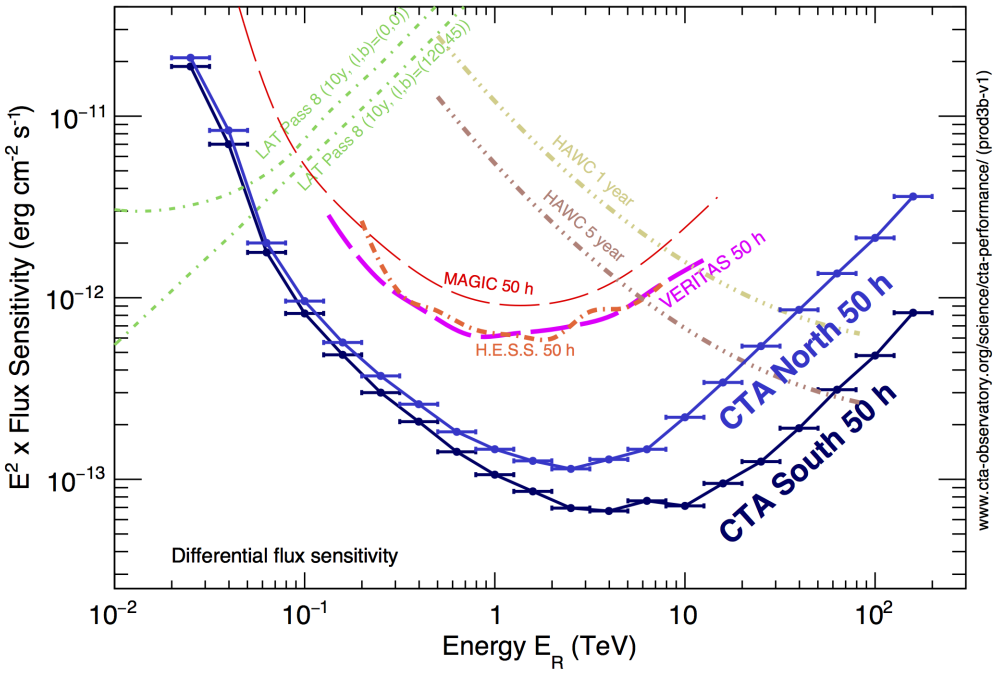

Figure 2.8: *Differential sensitivity of CTA compared with some other instruments. The analysis cuts in each bin have been optimized to achieve the best flux sensitivity to point-like sources. The IRF is provided for the observation time of 50 hours.* [28]

function of off-axis angle. CTA will have a sensitivity at the edge of its FoV equal to the on-axis sensitivity of current instruments [19].

The effects of NSB mainly affect the low part of CTA energy range. In the core of CTA energy range, not only the sensitivity but also the angular and energy resolutions are quite compatible with the results of dark sky observations [8].

The best overall performance is expected at around 1700 m site altitude. Higher altitudes improves performance below 50 Gev, while significantly decreasing performance above that energy (with differential sensitivity loss of $\approx 15\%$ at 3600 m) [13].

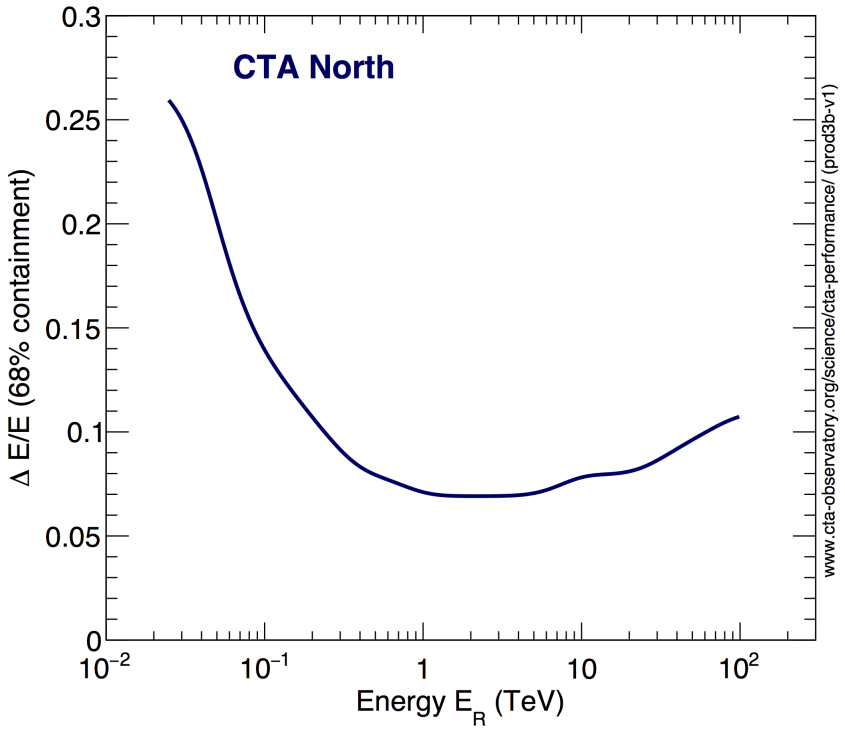

Figure 2.9: *The plot shows the energy resolution as a function of reconstructed energy for CTA-N. The angular cut is the same used for the calculation of the point source sensitivity.* [28]

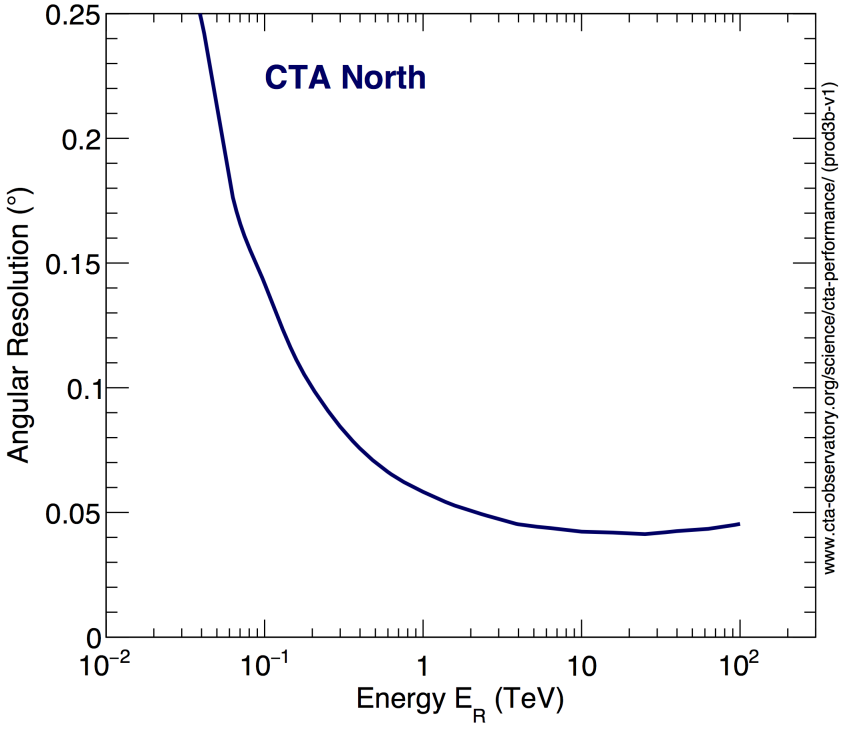

Figure 2.10: *The angular resolution vs. reconstructed energy curve for CTA-N.* [28]

Chapter 3

The atmosphere

The atmosphere is a wide layer of gases and suspended liquids and solids that entirely envelops our planet. Compared to the Earth's radius, however, the atmosphere is a very thin layer, only about 0.47% of the Earth's radius. The atmosphere has a mass of about $5.15 \cdot 10^{18}$ kg and its thickness decreases with increasing altitude. Three-quarters of the mass of the atmosphere is within 11 km of the Earth's surface. The atmosphere does not end abruptly but gradually becomes less thinner and disappears in the universe. There is no strict boundary between the atmosphere and outer space. However, the Kármán line, at 100 km above ground, is often used as the boundary between the atmosphere and outer space.

3.1 Composition of the atmosphere

Dry air contains 78.08% of nitrogen, 20.95% of oxygen, 0.93% of argon and other gases in small quantities, such as greenhouse gases, most of which are water vapor, carbon dioxide, methane, nitrogen oxides and ozone. Observations show that these gases are mixed in significantly constant proportions up to about 100 km altitude [5].

Various solid and liquid particles form an admixture in the atmosphere whose quantity varies constantly. Solid particles colloidally dispersed in the atmosphere that are the part of the atmosphere are called aerosols. Sources of aerosols can be natural and artificial and may be of organic and inorganic origin. In natural conditions, the atmosphere is never completely dry and clean. Some of the admixtures can make the atmosphere cloudy and humid. Natural sources (strong desert winds, forest fire, volcanic ash, floral pollen, spores, etc.) and artificial sources (especially in cities and industrial regions) can emit a large number of aerosol particles. Particles with 0.1 to 1.0 μm in diameter are highly effective in scattering solar radiation and those of

about 0.1 μm diameter are important in cloud condensation processes. [5] The average density of the atmosphere decreases from about 1.2 kg m^{-3} at the surface to 0.7 kg m^{-3} at 5 km.

3.2 The layering of the atmosphere

The atmosphere is subdivided into layers (atmospheric shells), in the vertical direction, according to the variation of temperature with altitude. The temperature profile is determined by atmospheric absorption of solar radiation, and the decrease of density with height [5].

Troposphere The troposphere is the lowest layer of the atmosphere lying on the Earth's surface and it contains 75% of the air mass. It is the lowest, densest and the hottest part of the Earth's atmosphere, with an average altitude of 10 to 12 km, ranging from 6 to 8 km at frigid zones and from 16 to 18 km at the equator. The difference in height is due to the fact that the air in the equatorial belt is exposed to increased solar radiation, therefore it is warmer what has a greater impact on air expansion (Gay Lussac's law). In the troposphere, the air temperature generally decreases with the height at a mean rate (so called **the lapse rate**) of about 6.5°C/km. The decrease is due to air is compressible - its density decreases with height, allowing rising air to expand and cool. The tropopause, the boundary layer between the troposphere and the stratosphere, is the level at which the lapse rate decreases to 2 °C/km or less ($\approx$ 0 °C/km). All meteorological events mostly take place in the troposphere and they are the consequences of the elevation of the warm layers of air and the descending of the colder layers of air, as well as the processes of cloud formation. The majority of EAS start and extend in the troposphere.

Stratosphere The stratosphere extends from 20 to 50 km of altitude and contains 10% of the air mass. Stratosphere contains most of the atmospheric ozone and reaches maximum density at about 22 km. However, the maximum temperatures associated with the absorption of UV radiation by ozone occur in the stratopause where they may exceed 0 °C [5]. The temperature rises with increasing altitude. The formation of clouds in the stratosphere is rare.

Mesosphere Above the stratopause, average temperatures decrease to a minimum of about –133 °C or around 90 km. The layer extending from 50 to 90 km is called the mesosphere and it is the coldes layer of the atmosphere. Pressure is very low in the mesosphere, decreasing from about 1 mb at 50 km to 0.01 mb at 90 km [5]. The

formation of clouds in this layer is rare, but some kinds of clouds such as noctilucent clouds can be formed but they have no impact on at all on the atmospheric transparency in the context of ground-based gamma-ray astronomy [14].

Thermosphere The thermosphere extends from 90 to approximately 600 km and it is characterized by large temperature fluctuations. Temperature rises with height due to the absorption of UV by O_2 and O_3 with a mean of about 700 °C.

Exosphere and magnetosphere The exosphere extends between about 500 km and 750 km and 1% of atoms are ionized. The number of ionized particles increases through the exosphere and, beyond about 200 km, in the magnetosphere, there are only electrons and protons derived from the solar wind. Satellites are usually placed in the exosphere.

To sum up:

- **pressure decreases** smoothly **with height** (at the surface is $\approx$ 1000 hPa),
- **temperature decreases with height** (the lapse rate is on average 6.5 °C/km, in the tropopause the lapse rate is negative),
- **density decreases with height** (at the surface is $\approx$ 1 kg m^{-3}).

3.3 Atmospheric instability and cloud formation

Clouds are the visible aggregate of minute particles of water and/or ice. Physically, a cloud is an aerosol. Clouds form when air rises and becomes saturated in response to adiabatic cooling. In order to form clouds there must be a sufficient supply of water vapor, aerosol particles, and a mechanism for lifting and cooling the air. Water, in condensed form, is the primary component of any cloud. The aresols provide the sites for condesation, making places where water vapor can adhere, so called **cloud condesation nuclei** . If temperature fall below the dew point and the concetration of water vapor exceed the equilibrium value, condensation can take its place.

There are four lifting mechanisms for cloud formation (Figure 3.1) :

- **Convection** - Short-term radiation emitted from the Sun causes the ground to warm up and the warm ground then emits long-term radiation that is absorbed by water vapor present in the atmosphere. The air at the surface of the Earth is warmed, it expands, becomes lighter and rises to higher heights (i.e. warm air

has a lower density than cool air, so warm air rises within cooler air). If the rising air cools to saturation, condensation and formation of water droplets may occur. The usual type of cloud that is formed by convection is the cumulus cloud.

- **Convergence** - Convergence occurs when there is a horizontal net inflow of air into a region [41]. When air converges along the earth's surface, the only place for it to go is upward. If the rising air cools down to the dew point, saturation and condensation occur and cloud droplets form.

- **Orographic Lifting** - Orographic lift occurs when an air mass is forced from a low elevation to a higher elevation as it moves over rising region [41], e.g. when air is pushed up against a mountain there is no place for the air to go but upward. The air is forced to rise and cools down adiabatically. There is a rise in the relative humidity over 100% and clouds can be formed.

- **Frontal Lifting** - A front is the boundary between two air masses, usually between a colder one and warmer one. When these two masses collide, the warmer mass, which is lighter, rises above the colder mass. As the air rises, it cools and its moisture condenses to produce clouds.

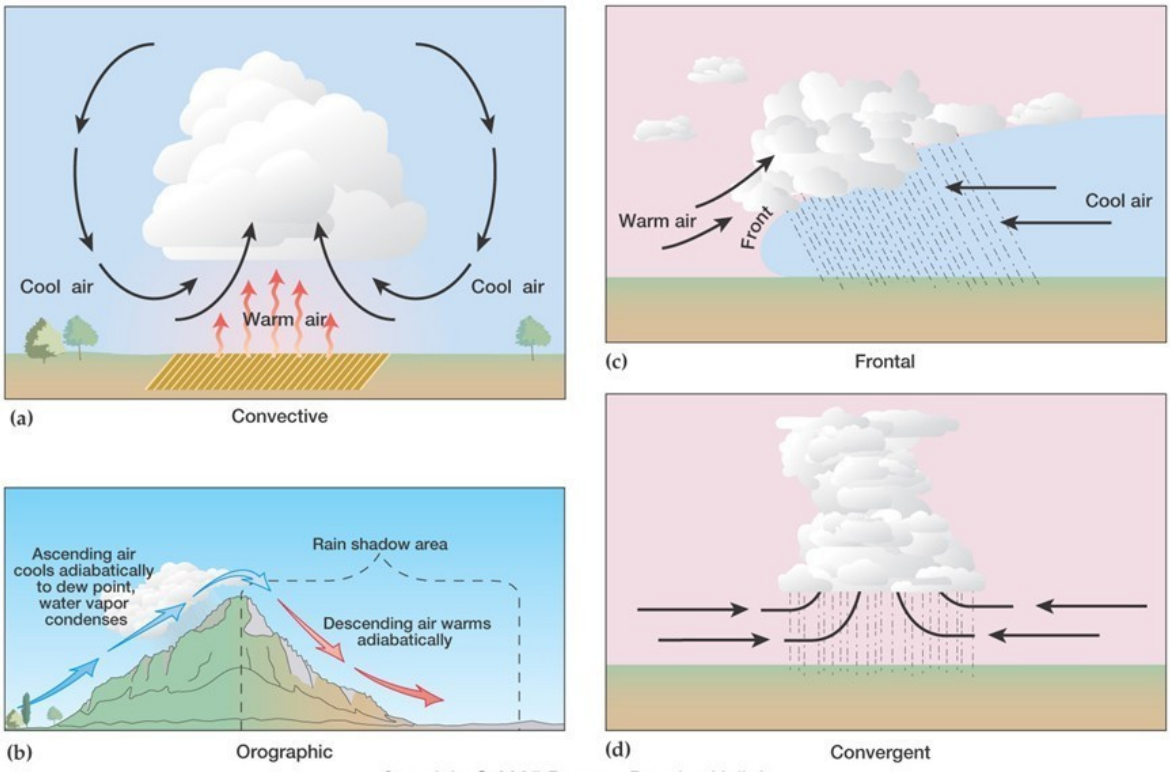

Figure 3.1: *Lifting mechanisms.* [36]

3.3.1 Adiabatic temperature changes

Consider **the air parcel**. We can think of it as a body of air with specific temperature and humidity characteristics, just like a ballon of air, that can expand and compress, while there is no mixing of parcel air with outside air. As air rises/sinks, the parcel expands/compresses and temperature decreases/increases. These temperature changes are only due to expansion and compression and therefore the process of cloud formation is an adiabatic process . Hence, regardless of the lifting mechanism, the rising air expands and cools adiabatically. Poisson's relations for adiabatic processes are given by:

$$Tp^{\frac{1-\gamma}{\gamma}} = \text{const.} \tag{3.1}$$

By using the ideal gas law we can derive other Poisson's relations:

$$TV^{\gamma-1} = \text{const}, \quad pV^{\gamma} = \text{const.}$$

Since for dry air $\gamma = 1.4 > 0$ it is obviously that as an air parcel rises and expands, its temperature must decrease. Also, the decrease of pressure cause its volume to increase and temperature to decrease [5] [iat]. When an air parcel adiabatically moves to a lower pressure environment, its volume increases. The latter involves work and the energy consumption what reduces the available heat and therefore the temperature decreases. Near the Earth's surface, the temperature changes are mostly non-adiabatic because of energy transfer due to changes in air characteristics during lateral motion and turbulence. However, if the air parcel moves vertically, the changes are adiabatic because the air is a poor heat conductor.

The rate at which temperature decreases in a rising, expanding air parcel is called **the adiabatic lapse rate** [5] . If there is no condensation, then the energy expended by expansion will cause the temperature of the mass to fall at **the constant dry adiabatic lapse rate (DALR)**. In Earth's atmosphere air pressure decreases at altitudes above Earth's surface, thus providing a pressure gradient force which counteracts the force of gravity on the atmosphere. Consider a cubic parcel with a density ρ, a height $\mathrm{d}z$, and a surface area $\mathrm{d}A$. The mass of the parcel can be expressed as:

$$m = \rho \mathrm{d}V = \rho \mathrm{d}z\mathrm{d}A.$$

Using Newton's second law, we have:

$$F = ma,$$

while the pressure can be expressed as:

$$\mathrm{d}p = -\frac{F}{\mathrm{d}A},$$

Using the above equations, we get:

$$\frac{\mathrm{d}p}{\mathrm{d}z} = -\rho g. \tag{3.2}$$

We can express equation 3.1 as:

$$\frac{\mathrm{d}T}{\mathrm{d}z} = \frac{\gamma - 1}{\gamma}\frac{T}{p}\frac{\mathrm{d}p}{\mathrm{d}z}, \tag{3.3}$$

and also the ideal gas law as:

$$\rho = \frac{p}{RT_s}. \tag{3.4}$$

where T_s denotes the temperature of the surroundings. The relation between the universal gas constant R and the specific gas constant R^* of a gas or a mixture of gases is given as the ratio of the specific gas constant and molar mass of the gas or mixture:

$$R^* = \frac{R}{M}. \tag{3.5}$$

Since molar mass of dry air is 28.9645 g/mol, the value ofR_d is equal to 287.058 J/kgK. Combining equations (3.2), (3.3) and (3.4) we have DALR equation:

$$\Gamma_d = -\frac{\mathrm{d}T}{\mathrm{d}z} = \frac{\gamma - 1}{\gamma}\frac{g}{R_d} = 9.8°\mathrm{C/km}.$$

However, continuous cooling of the air causes condensation and releases latent heat which neutralizes dry adiabatic temperature decrease rate to a certain level. Therefore, rising and the saturated air cools at a lower rate called **the saturated adiabatic lapse rate (SALR)**. The SALR varies over time and from place to place.

$$\Gamma_s = g\frac{R_d T^2 + L_v w T}{c_{pd} R_d T^2 + {L_v}^2 w \epsilon},$$

where $L_v = 2501000$ J/kg is the latent heat of vaporization of water, w is the mixing ratio of the mass of water vapour to the mass of dry air, T is the temperature of the saturated air and $c_{pd} = 1003.5$ J/kgK is the specific heat of dry air at constant pressure.

Before saturation, the rising air follows the DALR. After saturation, the rising air follows the SALR. Notice, while the DALR is a constant 9.8 °C/km, the SALR varies strongly with temperature. Since molar mass is 18.01 g/mol, acording to equation (3.5), the value ofR_v is equal to 461.5 J/kgK. Since the specific gas constant for dry air R_d is also R/M_d, it follows:

$$R_d M_d = R_v M_v,$$

thus:

$$\epsilon = \frac{R_d}{R_v} = \frac{M_v}{M_d} = 0.622.$$

At saturation the saturation mixing ratio is

$$w = \frac{\epsilon e_s}{p - e_s},$$

where where e_s is the saturation vapor pressure and $p = p_d + e_s$ is the total pressure and p_d the pressure due to the dry air component.

There is the third lapse rate, **the environmental lapse rate (ELR)** that is actual change in temperature with height, the rate at which the air temperature changes with height in the atmosphere surrounding a cloud or a rising parcel of air with a mean of 6.5 °C/km [39].

3.3.2 Air stability and instability

Atmospheric stability is one of the parameters that determine which type of cloud will form.

Figure 3.2: *Types of stability, respectively, stable, unstable and neutral.* [31]

Consider the ball that is placed in the bottom of the bowl as shown in Figure 3.2, left. The ball is in equilibrium. If we push the ball lightly, it will start moving from the bottom of the bowl to its top, and so several times. However, the ball will eventually come to the rest and return to the equilibrium position. We say that the ball is in a stable equilibrium. Now consider the ball place as shown in Figure 3.2, middle. When you push the ball, it will continue to move down the wall of the bowl and will never again come to its equilibrium position. We say the ball is in an unstable balance. Now consider the ball placed on the surface as shown in Figure 3.2, right. If the ball is given a slight push, the ball will move away from the equilibrium position. It will not, however, return to the equilibrium position, as in stable motion, nor will continue its motion as in the case of unstable motion. The ball is in neutral stability [31].

The air will be [5]:

- absolutely stable if ELR < SALR,
- absolutely unstable if ELR < DALR,
- conditionally unstable if SALR < ELR < DALR.

We should clarify the above conditions. If the air is lifted to any level in the atmosphere it will be cooler than the surrounding air at that level and will fall back to its original level if possible (it is cooler, hence, more dense and heavier) - it is absolutely stable. In the second case, as the air rises and cools, it is always warmer than the soundings, hence less dense and lighter. Therefore, it will continue to move upward in the atmosphere. This air is absolutely unstable. In the third case, as the air rises and cools in the atmosphere at the DALR, it is always cooler than the soundings, hence more dense than and heavier. Therefore, it will fall back to the initial height. This air is stable. If the air is forced to continue to rise, condensation begins and the air will cool at the SALR and rise to some level. At this level, the air is neutral because it will remain at this level if not forced to rise [26] [5].

The type of clouds that are formed in the stable air are the layered clouds (so-called *stratus* type of clouds) because a cloud is not forced to rise and instead it spreads out into layers. The type of clouds that are formed in unstable air are puffy (so-called *cumulus* type of clouds), because once displaced from its original position, the air continues to rise on its own. [26]

Obviously, cloud is formed when the humid air cools below the dew point temperature. The cooling of the air is accomplished by various processes described in the previous section. Apart from the humid air that cools down, so-called **condesation nuclei** are also important. Condensation nuclei are small, microscopic and hygroscopic particles (aerosols). As the air cools, water vapor condenses on those condensation nuclei. A large number of water droplets is formed and, hence, clouds. If they participate in the process of cloud formation, then we call them **cloud condesation nuclei (CCNs)**. There are three major sources of CCN [14]:

- salt particles from oceans (0.01 μm - 10 μm),
- sulphates from coil burning (a few 0.1 μm),
- soil particles from ground carried by wind (less than 10 μm).

The larger the size of a particle, the more readily it is wetted by water, and the greater its solubility, the lower will be the supersaturation at which the particle can serve as a CCN.

3.4 Cloud classification

Clouds can usually be divided into three groups according to the height at which they are located: **high clouds, middle clouds, low clouds** (Figure 3.3) [31].

High clouds were found at altitudes of 6 km above the ground and can be stretched all the way to the tropopause. These clouds are made up of ice crystals. The different types of high clouds are **cirrus** (a nearly transparent, white, fibrous or silky), **cirrocumulus** (a cirriform layer or patch of small white flakes arranged in groups or lines) and **cirrostratus** (a thin white veil of cirrus, nearly transparent; the Sun, Moon and stars can be seen through them).

Middle clouds are found at altitudes between 2 km and 6 km above the ground. These clouds are made up of water droplets, ice crystals, or both. The different types of middle clouds are **altocumulus** (puffy and scattered, from the ground they look very much like cirrocumulus cloud, may bulid upward), **altostratus** (uniform sheet or layer, can usually see the Sun through it; when becomes thick and rainy, it is called a nimbostratus cloud).

Low clouds are found at altitudes up to 2 km above the ground. These clouds are made up of water droplets. The different types of low clouds are **stratus** (look like fog, featureless gray to white sheets of cloud) and **stratocumulus** (a low, gray layer of clouds composed of globular masses or rolls).

Clouds of vertical development are found at altitudes all the way up to the tropopause. These clouds are made up of water droplets and ice crystals. The different types of these clouds are **cumulus** (dense with flat bases) and **cumulonimbus** (a cloud of great vertical development).

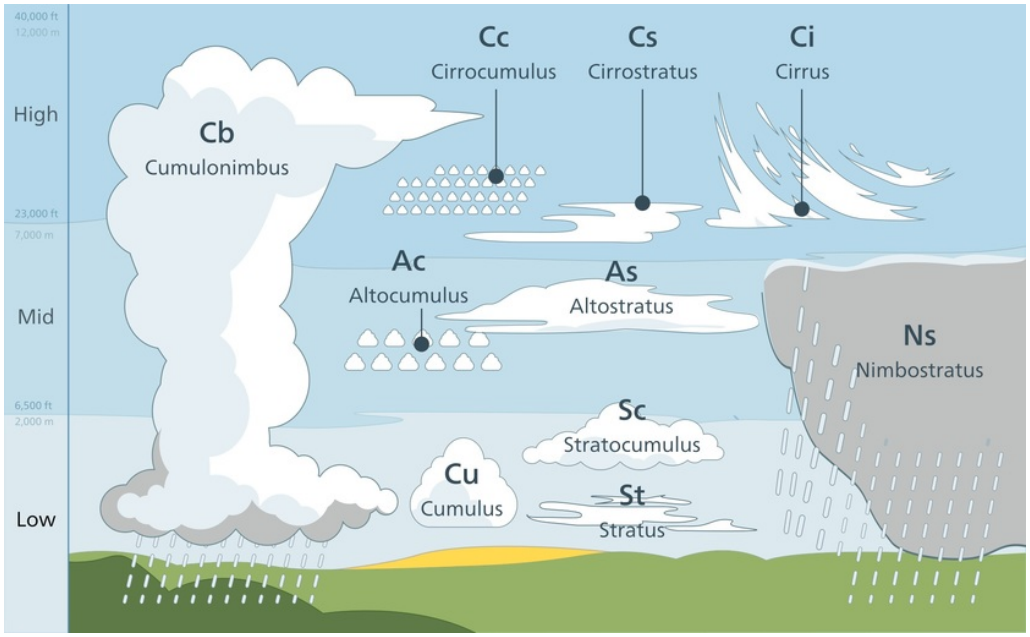

Figure 3.3: *Types of clouds. High clouds were found at altitudes of 6 km a.g.l. and can be stretched all the way to the tropopause. Middle clouds are found at altitudes between 2 km and 6 km a.g.l. Low clouds are found at altitudes up to 2 km a.g.l.* [35]

3.5 Cloud microphysics

3.5.1 Water clouds

Consider a spherical water droplet. The average radius of droplets in nonraining water clouds is ≈ 10 μm and the approximation of spherical particles satisfying. The assumption of a single droplet size (monodisperse clouds) is not realistic. Real clouds are polydisperse and contain a range of droplet sizes. Thus, we can consider a radius of a droplet r as a random value, which is characterized by **the cloud droplet size distribution** $n(r)$ normalized by the condition:

$$\int_0^\infty n(r)\mathrm{d}r = 1. \tag{3.6}$$

The integral:

$$N(r) = \int_{r_1}^{r_2} n(r)\mathrm{d}r \tag{3.7}$$

gives a fraction of droplets with radii between r_1 and r_2 in a unit volume of a cloud and it is called **the cloud droplet concentration** (total number density) . The function $n(r)$ is represented by the gamma distribution:

$$n(r) = Ar^\mu e^{-\frac{\mu r}{r_0}}, \tag{3.8}$$

where:

$$A = \frac{\mu^{\mu+1}}{\Gamma(\mu+1) r_0{}^{\mu+1}}$$

is the normalization constant and $\Gamma(\mu+1)$ is the Gamma function. The parameter μ characterizes the width of the cloud droplet size distribution $n(r)$. Moments of distribution are given by:

$$\langle r^n \rangle = \int_0^\infty r^n f(r)\mathrm{d}r = \left(\frac{r_0}{\mu}\right)^n \frac{\Gamma(\mu+n+1)}{\Gamma(\mu+1)}. \tag{3.9}$$

The above equation can be used to find, respectively, the average volume of droplets, the average surface area and the average mass of droplets:

$$\langle V \rangle = \frac{4\pi}{3} \int_0^\infty r^3 f(r)\mathrm{d}r,$$

$$\langle S \rangle = 4\pi \int_0^\infty r^2 f(r)\mathrm{d}r,$$

,

$$\langle m \rangle = \rho \langle V \rangle,$$

where $\rho = 1$ g/cm^3 is the density of water. r. It follows that:

$$\langle V \rangle = v_0 \frac{\Gamma(\mu+4)}{\mu^3 \Gamma(\mu+1)},$$

$$\langle S \rangle = s_0 \frac{\Gamma(\mu+3)}{\mu^2 \Gamma(\mu+1)},$$

$$\langle m \rangle = m_0 \frac{\Gamma(\mu+4)}{\mu^3 \Gamma(\mu+1)},$$

where

$$v_0 = \frac{4\pi {r_0}^3}{3}, \quad s_0 = 4\pi {r_0}^2, \quad m_0 = \rho v_0.$$

For the most used cloud model with $r_0 = 4\mu$m and $\mu = 6$. Although parameters are small, the very large numbers of cloud droplets (typically, 100 particles in cm^3) has an important impact on the atmospheric processes. For many practical applications, the optical properties of water clouds are parameterized as a function of the cloud droplet effective radius and liquid water content (LWC). **Cloud droplet effective radius** (or just effective radius) is an area weighted mean radius of the cloud droplets [42]:

$$r_{ef} = \frac{\langle r^3 \rangle}{\langle r^2 \rangle} = \frac{\int r^3 n(r) \mathrm{d}r}{\int r^2 n(r) \mathrm{d}r}.$$

The concentration of droplets N depends on the concentration C_N of CCNs. The value of CN is smaller over oceans than over continents, thus, the N is on average smaller in marine clouds. We can define **the dimensionless volumetric concentration of droplets** $C_v = N\langle V \rangle$. **The liquid water content (LWC)** is the measure of the mass of the water in a cloud:

$$C_w = \rho C_v,$$

or

$$C_w = N\langle m \rangle,$$

or

$$C_w = \frac{4\pi}{3} \rho \int n(r) r^3 \mathrm{d}r.$$

The liquid water path (LWP) a measure of the total amount of liquid water present between two points in the atmosphere and is defined as:

$$w = \int_{z_1}^{z_2} C_w(z) \mathrm{d}z,$$

where where $z_2 - z_1 = l$ is the geometrical thickness of a cloud. The geometrical thickness of a cloud depends on the cloud type. Some typical values are presented in Table 3.1.

Table 3.1: *Typical range of values N, C_v, and C_w in water clouds.* [15]

N (cm^{-3})	C_v (m^{-3})	C_w (g/m^3)
20-1000	10^{-7}-10^{-6}	0.01-1

3.5.2 Ice clouds

Microphysical properties of crystal (ice) clouds can not be characterized by a single particle size distribution due to extremely complex shapes of ice particles in ice clouds. Often shapes of ice crystals are columns, plates, dendrites, stellars, needles, sheaths, but combination forms of bullets and needles are also common [15]. The concentration of crystals N varies with height in the range from 50 to 50000 crystals/m^3. The ice water content is given by:

$$C_s = N\langle m \rangle,$$

where m is average mass of crystals in the range $10^{-4} - 10^{-1}$ g/m^3 [15]. Detailed characterization of ice clouds exceeds the framework of this paper.

Chapter 4

An introduction to atmospheric radiation

Consider the differential amount of radiant energy $\mathrm{d}E_\lambda$ passing through an area $\mathrm{d}A$ in time $\mathrm{d}t$, over a specified wavelength interval, λ to $\lambda + \mathrm{d}\lambda$ into a differential solid angle, $\mathrm{d}\Omega$. This energy is expressed in terms of the **monochromatic intensity** (or **radiance**) I_λ by:

$$I_\lambda = \frac{\mathrm{d}E_\lambda}{\mathrm{d}A\mathrm{d}t\mathrm{d}\lambda\mathrm{d}\Omega}.$$

The integral of the monochromatic intensity over some finite range of the electromagnetic spectrum is called the **intensity** (or **radiance**):

$$I = \int_{\lambda_1}^{\lambda_2} I_\lambda \mathrm{d}\lambda.$$

The attenuation of Cherenkov light (more generally, the attenuation of EMR) in the atmosphere occurs both due to absorption and scattering. Consider a beam of monochromatic photons all travelling in the same direction prependicularly at a slab[1] of atmosphere. As the beam passes through the slab, some will be absorbed and some will be scattered away from their initial direction - the intensity of the beam will reduce. This reduction of radiation intensity due to passing of radiation through the atmosphere is called **extinction** - the difference between outgoing and incoming radiation beams. Each of these contributions is linearly proportional to the intensity of the radiation at that point of absorption/scattering and the local concentration of the gases and/or particles. For each kind of gas molecule and/or particle that the beam encounters, its monochromatic intensity is decreased by:

[1] The atmosphere is usually approximated as plane-parallel in atmospheric remote sensing (also called slab geometry).

$$\mathrm{d}I_\lambda = -IQ_\lambda N\sigma \mathrm{d}x, \tag{4.1}$$

where N is the number of particles per unit volume of air, σ is the areal cross section of each particle, $Q_\lambda$is the (dimensionless) scattering or absorption efficiency, and $\mathrm{d}x$ is the differential path length. In the case of a gaseous atmospheric constituent $Q_\lambda N\sigma = \rho r k_\lambda$, where where ρ is the density of the air, r is the mass of the absorbing gas per unit mass of air, and k_λ is the mass absorption coefficient.

4.1 Atmospheric absorption

Absorption is the process by which incident radiation (i. e. energy) is retained by a substance, in this case, by the atmosphere. When the atmosphere absorbs energy, the result is an irreversible transformation of radiation into another form of energy according to the nature of the medium doing the absorbing. Absorption is mainly caused by three different atmospheric gases - water vapor causes the most absorption, followed by CO_2 and then O_3 (ozone).

From 290 to 600 nm, the absorption of light by ozone is the dominant absorption process. The UV absorption spectrum of the most abundant gas in the atmosphere consists of a band system from about 145 to 112 nm. The UV absorption spectrum of O_2 begins with the weak band between 260 and 200 nm, while below about 103 nm, O_2 absorption is in the form of an ionization continuum. The absorption of ozone spectrum begins with band between 200 nm and 300 nm centered at 255 nm. Ozone also shows weak absorption bands in the visible and near IR regions from about 440 nm to 1180 nm.

4.2 Atmospheric scattering

While absorption simply removes photons from a beam of radiation, scattering can change the beam direction, where it can be absorbed or scattered again. The intensity of the scattered radiation depends strongly on the wavelength λ and on the size and the shape of particle. For a spherical particle of radius d, scattering efficiency Q_λ in (4.16) can be presented as as a function of a dimensionless *size parameter* x:

$$x = \frac{2\pi d}{\lambda}, \tag{4.2}$$

and the relative index of refraction n (ratio of the refractive index of the particle and the refractive index of the surrounding medium). The effectiveness of

scattering depends on the size parameter. Geometric optics is when the particles get so big relative to the wavelength, thus we can calculate the particle-radiation interaction using basics optical principles (i.e. we can think of particle as a lens or prism), $x \leq>> 1$. For x between 0.1 and 50, we have Mie scattering. (the particle size is comparable to the wavelength), and for $x << 1$, we have Rayleigh scattering (strongly dependent on the wavelength of radiation). The Rayleigh scatering by molecules in the atmosphere and the Mie scattering by aerosols, haze and **clouds** are the most important fot the attenuation of Cherenkov light [14].

4.2.1 Rayleigh scattering

Rayleigh scattering is the scattering of light by particles smaller than the wavelength of light. Typical size of the air molecules is 0.2 nm and the detectable wavelengths of Cerenkov light range from 290 nm to 600 nm, thus:

$$\frac{d_{molecules}}{\lambda_{Cherenkov}} \approx 10^{-3}.$$

The relationship between the intensity of light I_λ in Rayleigh's regime and the wavelength λ of light and the particle radius d is given by:

$$I_\lambda \propto d^6/\lambda^4.$$

Consider a small homogeneous spherical particle whose radius d is much smaller than the wavelength λ of the incident radiation $\vec{E}_0$. The electric field of incident radiation induces dipole moment of the particle $\vec{p}_0$. Thus, according to classical electromagnetic theory we have:

$$\vec{p}_0 = \alpha \cdot \vec{E}_0, \tag{4.3}$$

where α is the polarizability of the particle. The scattered field at a distance r from a dipole is

$$E = \omega \alpha E_0 e^{i\omega t},$$

that is

$$\vec{E} = \frac{\omega^2}{c^2 r} \exp\left[i\omega \left(t - \frac{r}{c} \right) \right] \vec{r} \times (\vec{p} \times \vec{r}),$$

where c is the speed of light and r is large enough to be in the far field of the dipole. One can find (e. g. [17]) that the intensity of the scattered light, assuming that the incident light is unpolarised, is given by

$$I = \frac{\alpha^2 \omega^4}{c^4 r^2}(1 + \cos^2_\theta) I_0.$$

4.2.2 Mie scattering

If the scatterers are large compared to the wavelength of light then geometric optics provide a good approximation. However, in most atmospheric situations aerosols are neither large nor small enough to be treated *that* simply. This problem was first solved in 1908 by Gustav Mie. Mie determined the wave vector in spherical coordinates for EM waves, specified by Maxwell's equations. Mie scattering is caused by pollen, dust, smoke, water droplets (clouds), and other particles in the lower portion of the atmosphere. The typical size of water droplets in cloud is 10 μm, therefore:

$$\frac{d_{droplet}}{\lambda_{Cherenkov}} \approx 10.$$

Mie scattering results in white clouds with black bottoms when the clouds are tall enough. When all visible light is scattered by cloud, the cloud turns black.

4.3 Local optical characteristics of cloudy media

The attenuation of a direct light beam with the intensity I_0 in a cloudy medium is given by:

$$I = I_0 e^{\frac{-\tau}{\cos\theta_0}},$$

where I_0 is the intensity of an incident light, I is the intensity of the transmitted direct light, θ_0 is the solar zenith angle.

$$\tau = \int_0^H \sigma_{ext}(z)\mathrm{d}z,$$

is the optical thickness (optical depth) of a cloud, H is the geometrical thickness of a cloud and σ is the extinction coefficient with the assumption that a cloud is contained inside horizontally infinite homogeneous plane-parallel layer. The reciprocal of σ is called the photon free path length - the average distance between photon scattering events in the cloud. Knowing the average number of scattering events n, we can find the average distance photon travels in the medium before escape $L = ln$ and the average total time which photon spends in a cloud $T = L/c$, where c is is the average speed of light in a cloudy medium [15].

The extinction coefficient varies with the height in a cloudy medium :

$$\sigma_{ext} = \int_0^\infty N f(a) C_{ext} \mathrm{d}a, \tag{4.4}$$

where N is the number concentration of particles, C_{ext} is the extinction cross section given by:

$$C_{ext} = \Sigma/2, \tag{4.5}$$

where Σ is the surface area of a droplet.

N is related to the volume concentration of particles C_V by the equation:

$$N = \frac{C_V}{\langle V \rangle}. \tag{4.6}$$

where

$$\langle V \rangle$$

is the average volume of particles. Thus, from (4.4), (4.5) and (4.6) it follows:

$$\sigma_{ext} = \frac{3C_V}{2a_{ef}},$$

where $a_{ef} = 3\langle V \rangle / \langle \Sigma \rangle$ is the effective radius. The extinction coefficient can be also expressed via the liquid water content C_w:

$$\sigma_{ext} = \frac{3C_w}{2\rho a_{ef}},$$

where ρ is the density of water. The above equation is valid only in the visible range of the EM spectrum, calculations for larger wavelengths should be performed with the Mie theory.

The probability of photon absorption β is defined by:

$$\beta = \frac{\sigma_{abs}}{\sigma_{ext}},$$

where σ_{abs} is the absorption coefficient given by:

$$\sigma_{abs} = \int_0^\infty N f(a) C_{abs} \mathrm{d}a,$$

and C_{abs} is the absorption cross section. Thus, for the scattering coefficient it follows:

$$\sigma_{sca} = \sigma_{ext} - \sigma_{abs}.$$

To characterize the relative importance of scattering and absorption in a medium, the single scatter albedo is used:

$$\omega = \frac{\beta_{sca}}{\beta_{ext}} = \frac{\beta_{sca}}{\beta_{sca} + \beta_{abs}}.$$

The optical depth expresses the quantity of light removed from a beam by absorption or scattering during its path through a medium (if $\tau \approx 0.5$, transmissivity is $\approx 60\%$).$If\, \tau << 1$, the medium is optically thin. In the optically thin regime, the amount of extinction is linearly related to the amount of material.

If $\tau >> 1$, the medium is optically thick. Thus, photon will interact many, many times with particles before its escape. Any photon entering the cloud will have its direction changed many times by scattering - we can see nothing at all through the cloud.

If the same particles are doing both absorbing and scattering, and they usually do, then:

$$\rho_{abs} = \rho_{sca} = \rho$$

and eq. (4.1) can be written as:

$$\frac{\mathrm{d}I}{I} = -\beta_{ext} \cdot \rho \mathrm{d}a. \tag{4.7}$$

Equation (4.7) has the solution:

$$I = I_0 \cdot e^{-\tau}, \tag{4.8}$$

where $\tau = \int_0^z \rho \cdot \beta_{ext} \cdot \mathrm{d}z$ is another form of optical depth equation, while z measures distance along the path of the beam, with $z = 0$ at the point of the beam entry. Optical depth describes how much absorption/scattering occurs when light travels through an absorbing/scattering medium. Obviously, radiance exponentially decreases after entering in abosrbing/scattering medium. The latter equation is nothing but Bouguer-Beer-Lambert's law. Generally, β_{ext} will change with postion, but for the cases where β_{ext} changes slowly we can write:

$$\tau(z) = \beta_e \cdot u(z),$$

where $u(z)$ is the mass path - the mass of absorbers in a tube of length z and unit cross section, coaxial with the beam. The amount of atmospheric extinction depends on the altitude of an object, being lowest at the zenith and at a maximum near the horizon.

The transmittance (transmissivity) of the slab is defined as the fraction of the outgoing and incoming intensity :

$$\mathcal{T} = \frac{I(x)}{I(0)} = e^{-\tau}.$$

The absorptance (absorptivity) A is the fraction of the incoming intensity absorbed by the slab:

$$\mathcal{A} = 1 - \mathcal{T}.$$

Chapter 5

Data analysis

For the observation of high energy particles, a calorimetric principle is required. The natural calorimeter for cosmic HE particles is the atmosphere. While for the most astronomers the atmosphere is an aggravating factor, for γ-ray ground-based astronomy the atmosphere is an integral part of the detector. To make the observations consistent and accurate, we need a clean atmosphere. Of course, this is not always the case because there are aerosols, clouds and other disturbances in the atmosphere. The term extinction stands for the intensity of light decrease when the light is passing through the atmosphere. Extinction occurs due to attenuation (absorption and scattering) in the atmosphere and is proportional to the air mass and the atmospheric pressure. The main cause of extinction is scattering, and the most critical is Mie's scattering. The extinction is very variable, even on the one hour scale [14].

The atmosphere is an important part of Cherenkov imaging telescope, so the telescope response depends on the unpredictable atmospheric changes. Since there is no test-beam for Cherenkov telescopes, the calibration is entirely based on Monte Carlo simulations (MC). MC simulations are usually made in two steps [14]:

- simulation of particle showers in an atmosphere caused by the invasion of cosmic rays (charged particles), cosmic γ-rays or cosmic neutrinos, and
- detector simulations.

The first part of the simulation is common to all γ-ray astronomy experiments. The second part is specific to each experiment. In the energy range from 10 GeV to 100 TeV, the first interactions of the primary cosmic particle with particles in the atmosphere start on average at 22 km a.s.l. In the case of high clouds like cirrus, Cherenkov photons are mostly produced below the clouds, and clouds do not affect them. However, in the case of low clouds, Cherenkov photons are produced above the clouds, whereby a fraction of information about the primary particle that initiated a

shower may be lost. Typical clouds above La Palma can be sufficiently transparent to allow the observations. A combination of lidar measurements and transmittance simulation can improve the data quality and increase the duty cycle.

Most of the showers in the atmosphere, initiated by the cosmic rays, begin and stretch into the troposphere. Sometimes, shower begins in the stratosphere, but most of Cherenkov light vanishes in the troposphere. Moreover, practically all clouds lie in the troposphere. The atmosphere is too large and too complex, so we are not able to fully describe it. However, approximate models are used instead. The most commonly used model of the atmosphere is the U.S. Standard Atmosphere 1976.

The Observatory Roque de Los Muchachos (ORM) on the Canary Island of La Palma is a great place for astronomical observations. Low clouds remain almost always below the mountain peaks and they are not included in the MC simulation. Since high clouds, cirrus, are thin and scattered, and mostly above the altitude at which the majority of Cerenkov photons is produced, neither are them included in the MC simulations. There are only middle clouds left, of which, in our opinion, just altostratus could have a measurable impact on the atmospheric transmission. Altocumulus are scattered clouds, which is why particles shower can just pass through the cloud or miss it. In that case, we will have a weak and distorted photo that will probably be cut off in the data analysis. The MC simulations for a uniform, 1 km thick altostratus are made. For ORM (placed at 2200 m), lower altostratus (below 3000 m) can be treated as a fog, and during foggy weather, observations are not performed anyway. Therefore, only the altostratus cloud with the base at 3000 m or more, are considered [14].

The motivation to this Master's thesis was to examine the influence of atmospheric transmission on the quality of data observed with Cherenkov telescopes. Since cloud layers and corresponding atmospheric transmission are quickly changing on La Palma where CTA-N is placed, good atmospheric models are important for efficient adaptive (dynamic) observation scheduling.

5.1 Metodology

In order to examine the influence of cloud altitude and optical depth on CTA-N performance, transmittance simulations for the atmosphere with cloud were made. The cloud simulations were done with MODRAN computer program. For each wavelength and each altitude, MODTRAN produced a single number - transmittance. Transmittance simulations were made according to the *Proposal for the gamma-ray simulation campaign for the CTA-N* that suggests six sets of data with different AOD and cloud base height (see Table 5.2) [12]. The final output file is a large table of

transparencies with default filename extension M5. After the transmittance simulations were made, our own Python code was used to transform a table of transparencies (M5 file) into a table of atmospheric optical depths (AOD, .dat file) appropriate as input for `sim_telarray`. Obviously, we've made some modifications of `sim_telarray`. Instead of using a default file with optical depths for a clear atmosphere, simulated AODs that include clouds were used. Therefore, the atmospheric models produced by MODTRAN can be used as inputs for Monte Carlo simulations with `sim_telarray`.

5.1.1 Transmittance simulation with MODTRAN

MODTRAN (**MOD**erate spectral resolution atmospheric **TRAN**smittance algorithm and computer model) is a computational radiation transfer algorithm that is used to model the spectral absorption, transmission, emission and scattering characteristics of the atmosphere, developed by the Air Force Research Labs in collaboration with Spectral Sciences, Inc. [6].

Modeling of mentioned parameters is accomplished by modeling the atmosphere as a set of homogeneous layers. The characteristics of these layers can be user provided or the internal model of the atmosphere can be used (urban or rural, equatorial or arctic, etc). The atmosphere is modeled via constituent vertical profiles, both molecular and particulate [49]. MODTRAN solves the radiative transfer equation including the effects of absorption, emission, scattering, surface reflections and emission, solar/lunar illumination, and spherical refraction. The MODTRAN software computes atmospheric spectral transmittances and radiances for wavelengths > 0.2 μm.

For each wavelength and each altitude, MODTRAN produced a single number - transmittance. The final output file is a large table of transmittancies with default filename extension .M5. After the transparencies simulations were made, our own Python code was used to transform a table of transparencies (.M5 file, Figure 5.1) into a table of atmospheric optical depths (AOD, .dat file) appropriate as input for `sim_telarray`. We have used MODTRAN 5.2.2 version installed at `warp.zeuthen.desy.de`. Parameters for the simulations were used according to the *Proposal for the gamma-ray simulation campaign for the CTA-N* [12].

The clouds were assumed to be grey, i.e. the extinction coefficients are independent of wavelength, with a thickness of 1 km and the Ångström index of zero. The altitude dependency of a cloud can be very complex, however, it was assumed that they are thin, while the internal structure of cloud was neglected, thus, a uniform extinction throughout the cloud served as a good approximation. Used heights of cloud base ranged from 3000 m to 13000 m above ground level (in the steps of 2000 m).

```
#============================
#
# MODTRAN options as follows:
#
# Atmospheric model: 1 (Tropical atmosphere)
# Haze: 10 (DESERT extinction, VIS is wind speed dependent)
# Season: 0
# Vulcanic dust: 0
# Zenith angle:  0.00 deg
# End altitude: 2.147 km
# Ground altitude: 2.147 km
#
#============================

# H2= 2.147, H1= 2.197 2.247 2.347 2.447 2.647 2.847 3.147 3.647 4.147 4.500 5.000 5.100 5.200 6.500
7.000 8.000 9.000 10.000 11.000 12.000 13.000 14.000 15.000 16.000 18.000 20.000 22.000 24.000 26.000
28.000 30.000 32.500 35.000 37.500 40.000 45.000 50.000 60.000 70.000 80.000 100.000

203.000 0.76493943 0.76637381 0.59060854 0.59495813 0.36172411 0.37207454 0.23867767 0.10351360
0.11906959 0.24093719 0.14802659 0.16660692 0.18641421 0.04739407 0.75304729 0.75587398 0.75866920
0.76143795 0.76417714 0.76688701 0.76956916 0.77222264 0.77484995 0.77744871 0.78005093 0.78266060
0.78523660 0.78779018 0.79031134 0.32296818 0.12928621 0.16723396 0.20989013 0.25711104 0.30680701
0.35847098 0.41293526 0.24494493 0.35017177 0.44292173 0.50387484 0.55043846 0.61148661 0.66696626
0.67986906 0.76505631 0.83582419 0.89085984 0.88871598 0.95326746 0.96810848 0.99226141 0.99812996
0.99958837
204.000 0.76557547 0.76700687 0.59157759 0.59592330 0.36287951 0.37323582 0.23976618 0.10427072
0.11989662 0.24206433 0.14896600 0.16760883 0.18747534 0.04789307 0.75378478 0.75660580 0.75939572
0.76215845 0.76489210 0.76759690 0.77027345 0.77292061 0.77554232 0.77813530 0.78073180 0.78333527
0.78590590 0.78845322 0.79096854 0.32426608 0.13023619 0.16831115 0.21106467 0.25834963 0.30807588
0.35973212 0.41414952 0.24576557 0.34950870 0.44053537 0.49955538 0.54462302 0.60529053 0.66072547
0.67344844 0.75997931 0.83217853 0.88849777 0.88664967 0.95262867 0.96786267 0.99225765 0.99813348
0.99958825
```

Figure 5.1: *Output of MODTRAN - a table of atmospheric transparencies vs. altitudes vs. wavelengths (+ some shell scripts). NOTE: Figure does not show the entire file.*

Proposed and used total AODs were 0.05, 0.1, 0.2, 0.3, 0.5, 0.7.

Details of used parameters can be found in the Table 5.1., while simulation scenario according to *Proposal for the gamma-ray simulation campaign for the CTA-N* can be found in the Table 5.2. For each set, i.e. for each cloud which is a part of that particular set, transmittances simulations have been made. Transmittances are converted to AODs using the Python code that can be found at the end of this thesis. For every single cloud, the difference between the AOD for the atmosphere with cloud and the AOD for clear atmosphere was found. Graphical representations of AOD difference vs. cloud base altitude were also made.

Table 5.1: *Some of the MODTRAN settings.* [22][10]

Parameter	**Value**
Wavelengths range	203 nm to 999 nm (step 1 nm)
Atmospheric model	6 (US Standard Atmosphere)
Extinction model	10 (desert extinction)
Zenith angle	0.0°
Ground altitude	2147 m

Table 5.2: *Details for each individual simulation scenario.* [12]

Set NO.	Cloud NO.	Height of cloud base a.g.l. (m)	Total AOD
1	15-20	3000, 5000, 7000, 9000, 11000, 13000	0.05
2	21-26	3000, 5000, 7000, 9000, 11000, 13000	0.1
3	27-32	3000, 5000, 7000, 9000, 11000, 13000	0.2
4	33-38	3000, 5000, 7000, 9000, 11000, 13000	0.3
5	39-44	3000, 5000, 7000, 9000, 11000, 13000	0.5
6	45-50	3000, 5000, 7000, 9000, 11000, 13000	0.7

5.1.2 CORSIKA and `simtel_array`

Any simulation of the IACT technique consists of two major components [14]:

- the development of the EASs and emission of Cherenkov light by the shower particles, and
- the detection of Cherenkov light and recording of signals by the instruments, i.e. detector simulation.

The first major component is based on the CORSIKA program, a computer softwer for simulations of EASs induced by high energy CRs. The second major component, termed `simtel_array` implements all the details of the detectors, such as optical raytracing of the photons, their registration by photomultiplier tubes, switching of discriminators or comparators at the pixel level and at the telescope trigger level, digitization of the resulting signals [7].

CORSIKA

Monte Carlo (MC) methods (or Monte Carlo experiments) are a broad class of computational algorithms that rely on repeated random sampling to obtain numerical results that are used for modeling of physical systems. The main component of each Monte Carlo method are random numbers, i.e. numbers that appear in the uncorrelated order.

CORSIKA (**CO**smic **R**ay **SI**mulations for **KA**scade) is a computer software for simulation of EASs induced by high energy CRs. For shower construction after interaction of HE particle with the atmosphere, Monte Carlo simulation and knowledge of strong and electromagnetic interactions are used. Because of incomplete knowledge and execution time, programs of this type use numerous approximations. CORSIKA

was originally developed to perform the KASCADE experiment at Karlsruhe. CORSIKA applications range from energies of 10^{12} eV to the highest energies observed of 10^{20} eV.

Photons, light nuclei and many other particles can be treated as primaries. The trajectories of the particles through the atmosphere are followed up to their interactions with particles in the atmosphere or, in the case of unstable particles, until their decay. The hadronic interactions at LE can be described by few reaction models such as GHEISA (the recommended model for LE hadronic interaction designed for laboratory energies up to a few hundred GeV [14]), FLUKA, UrQMD. The hadronic interactions at HE can be described by five reaction models: VENUS (mainly designed to treat nucleon-nucleon, nucleon-nucleus, and nucleusnucleus scattering at ultrarelativistic energies [14]), QGSJET, DPMJET, SIBYLL, and HDPM. For the electromagnetic interaction, EGS4 and NGK model are used.

CORSIKA is operated with the pseudo random number generator RANMAR able to generate simultaneously up to $9 \cdot 10^8$ independent sequences and it satisfies very stringent tests on randomness and uniformity.

The EGS4 enables full MC simulation of the electromagnetic component of showers. Charged particles (in this case, mostly electrons and positron) emit Cherenkov radiation if travel through the medium with speed v greather than the local speed of light, which is given by the local refractive index n and the vacuum speed of light c. With every step of the propagation through the atmosphere, the condition:

$$\frac{nv}{c} > 1$$

is tested. The local refractive index can be approximated by the local density $\rho(h)$ (in g/cm^3):

$$n = 1 + 0.000283 \cdot \frac{\rho(h)}{\rho(0)}.$$

The wavelength dependency is neglected. Photon number N_C emitted per path length s at an angle θ_C is calculated to:

$$\frac{\mathrm{d}N_c}{\mathrm{d}s} = 2\pi\alpha \int \frac{\sin^2\theta_c}{\lambda^2}\mathrm{d}\lambda$$

where α is fine structure constant and $\theta_c = \arccos(c/nv)$. Integration boundaries are defined by the wavelength band within which the Chernekov detector is sensitive.

Before the program is started, in the input file shower parameters are defined. γ-photon, electron and proton are defined as primary particles in separate simulations. Electrons, protons and night sky are treated as background and differ from aimed

events according to the shape of signal in the camera. Other parameters are, for example, the ranges of the zenith and azimuth angle, the height of the first interactions, the first target, the atmospheric model, atmospheric parameters for a single layer, layer boundaries etc. The mentioned parameters determine density in a single layer, while almost entire interactions of interest depend on density. Neutrinos interactions are neglected because of the extremely small cross section and are assumed to have a free pass through the atmosphere.

Atmospheric absorption of Cherenkov photons is neglected by default, but can be considered later by writing the origin height of each photon bunch onto the Cherenkov output.

SIM_TELARRAY

This program was originally developed for simulating the HEGRA telescope system and then adapted to H.E.S.S. `sim_telarray` is a program package for the simulation of arrays of IACTs. Its input data consists of Cherenkov light simulated with the CORSIKA [7]. It is the main simulation package for the CTA.

`sim_telarray` uses data produced by CORSIKA and traces the photons from their point on the sphere to the camera focal plane. The surviving photons are converted to electronic signal depending on the input photon detection efficiency (PDE) and single photo-electron (SPE) response, triggered, digitized and read out. The main inputs for `sim_telarray` are configuration files that represent the optics and camera of the telescope. The shadowing of the structure, the mirrors reflectivity and the angular acceptance of detectors or any windows are also taken into account. Using `sim_telarray`, each telescope can be configured separately on the command line and via configuration files.

A tables with optical depths obtained by MODTRAN are used instead of default `sim_telarray` file. Simulations were made for 4 LSTs configuration presented on Figure 2.6 since numerous of researches show that the differential sensitivity curve is placed lower in the case of four telescopes rather than in the case of three telescopes (e.g. see [25]). Simulations were produces by supercomputer "Bura" at University of Rijeka. In order to test the analysis chain, we produced preliminary MC simulations using `sim_telarray` with low statistics (γ: 1971975, e^-: 83202, p^+: 212931). Some of used parameters were: zenith angle 20°, azimuth angle 180°, Standard Wobble, observatory level 2147 m.

5.2 Results and discussion

MODTRAN results

Figures 5.2 to 5.5. are selected plots of AOD difference vs Altitude. Plots are based on the data produced by MODTRAN. Those are actually check-plots to make sure that data produced by MODTRAN is really for that particular cloud.

On the y-axis AOD difference values for the atmosphere with clouds and clean atmosphere are laid. On the x-axis altitude values are laid. The dashed green line represents the AOD for that particular case, while dashed red lines are the boundaries of the cloud.

Each point of the graph shows the AOD difference as an overall effect of the atmosphere all the way from the telescope to some altitude. Since clouds are defined as a 1 km thick layers, thus, the AOD difference is equal to zero all the way from the telescope level to an altitude at which the bottom edge of the cloud is placed. As we enter the cloud (i.e. with an altitude increase), the AOD difference is getting bigger. Since the cloud density is constant, the optical depth increases linearly up to the top edge of the cloud. At altitudes higher than the altitude at which the cloud is placed, the difference becomes constant again. At those altitudes, a contribution of the cloud to AOD difference is accounted as well.

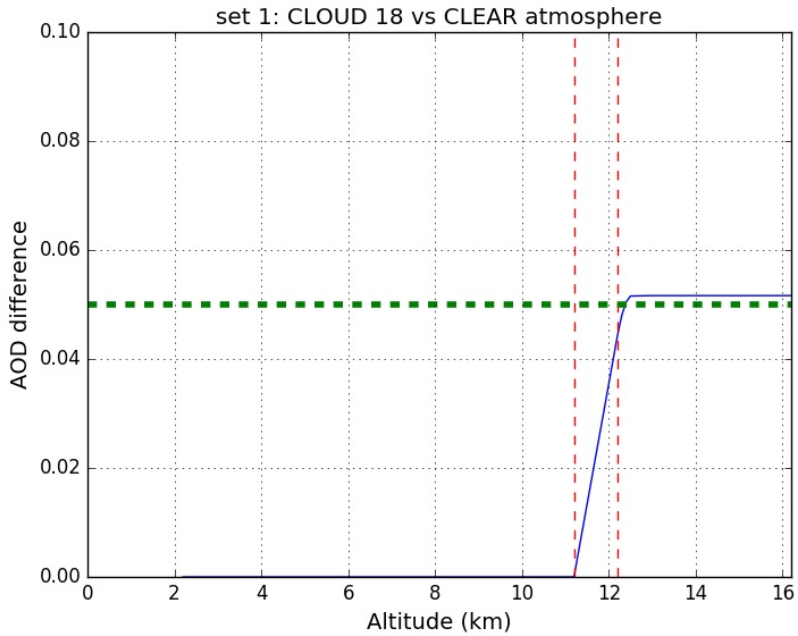

Figure 5.2: *AOD difference of cloudy and clear atmosphere vs Altitude, for SET1 (total AOD 0.05); #18 (height of cloud base 9 km a.g.l.).*

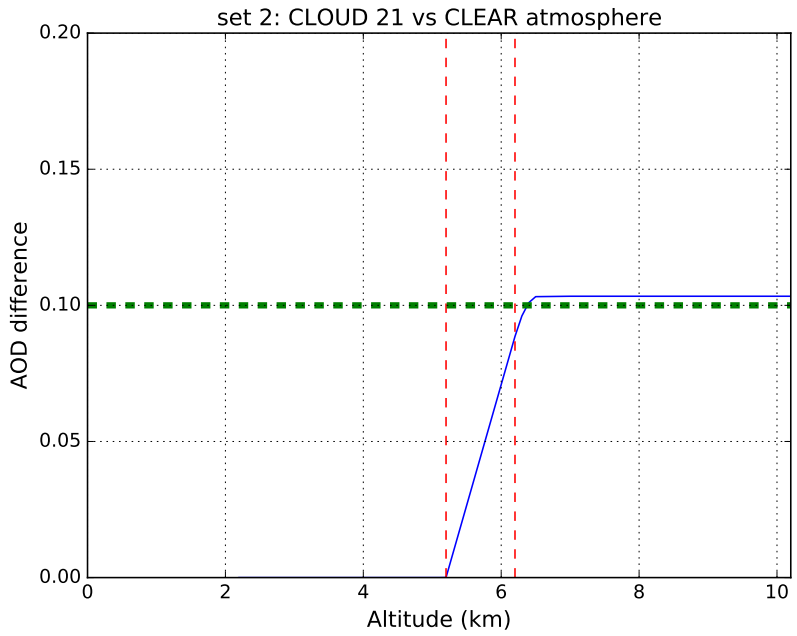

Figure 5.3: *AOD difference of cloudy and clear atmosphere vs Altitude, for SET2 (total AOD 0.1); #21 (height of cloud base 3 km a.g.l.).*

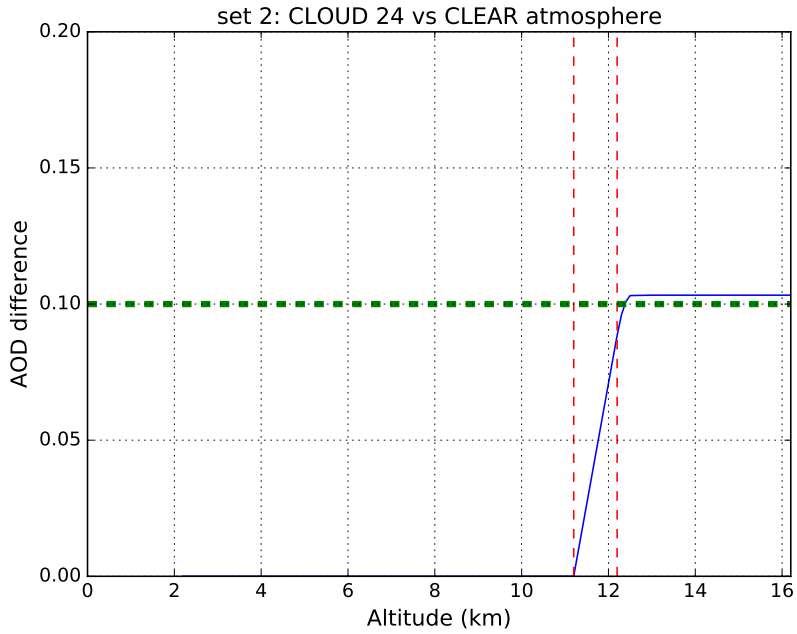

Figure 5.4: *AOD difference of cloudy and clear atmosphere vs Altitude, for SET2 (total AOD 0.1); #24 (height of cloud base 9 km a.g.l.).*

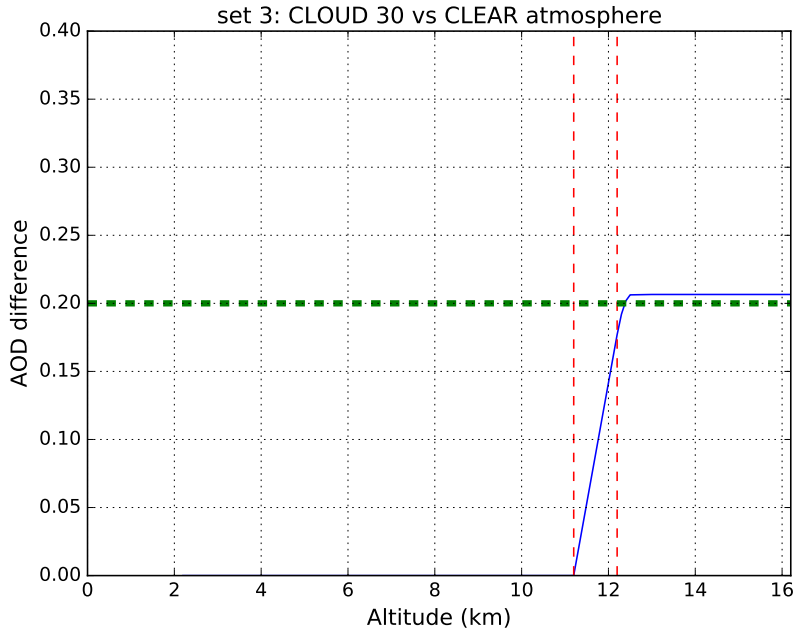

Figure 5.5: *AOD difference of cloudy and clear atmosphere vs Altitude, for SET3 (total AOD 0.2); #30 (height of cloud base 9 km a.g.l.).*

MC results

The differential sensitivity shown in figures below is defined as the minimum flux needed by the LST telescope to obtain a 5-standard-deviation detection of a point-like source, calculated in non-overlapping logarithmic energy bins (five per decade) [28]. At least ten detected gamma rays per energy bin are required [11]. To achieve the best flux sensitivity to point-like sources, the analysis cuts in each bin have been done. The instrument response functions (IRF) are provided for 5 hours observation time. Differential sensitivity corresponds to an independent detection in each energy interval (energy bin) and is much more strict than the integral sensitivity, i.e. differential sensitivity is an integral sensitivity in small energy bins [11].

For the significant detection of a gamma-ray point-like source, the five-standard-deviation (5σ) statistical significance ($S \geq 5$) and the presence of at least ten excess events above background are required ($N_\gamma \geq 10$, and $N_\gamma/N_{bg} \geq 0.05$ where N_{bg} denotes background in the source regions) [8]. For calculating the statistical significance of a gamma-ray signal above some background, one can use eq. 17 of [16]. For the differential sensitivity, we apply these requirements for each energy interval (usually five intervals per decade of reconstructed energy, i.e. intervals of the decimal exponent of 0.2). For the integral sensitivity, requirements are applied just for the total signal and background. Integral sensitivity does not show the actual energy regime where an

assumed power-law spectrum is most significant and heavily depends on the assumed spectral index. Differential sensitivity depends on the bin size [8].

The angular resolution vs. reconstructed energy curve shows the angle within which 68% of reconstructed gamma rays fall, relative to their true direction, or the angular radius from a point-like source that contains 68% of the events [8]. γ-hadron separation cuts are applied for the MC events used to determine the angular resolution.

The energy resolution is obtained from the distribution of $(E_R - E_T)/E_T)$, where R and T refer, respectively, to the reconstructed and true energies of gamma-ray events recorded by the telescope. The energy resolution is the half-width of the interval around $E_R/E_T = 1$ which contains 68% of the distribution. Higher resolution is possible at the expense of collection area.

The differential sensitivity (minimum detectable flux from a point-like gamma-ray source) depends on the collection area, angular resolution, and rate of background events surviving all gamma selection cuts.

At medium energies, the sensitivity is quite good. However, at low energies there is a visible effect of the clouds. The latter was expeceted. The telescopes are most sensitive at the energy threshold where the primary particle energy is low. If the attenuation of radiation is considerable, then with such small number of Cherenkov photon, a image reconstruction is aggravated. Therefore, there must be an impact on the telescope at LE levels due to Cherenkov radiation absorption and scattering in the atmosphere.

Effective area get reduced with respect to the clear atmosphere, the more the lower the shower energy. The reduction is visible below a certain energy higher than the threshold. Above that energy, effective areas gradually approach the clear atmosphere case at the highest energies.

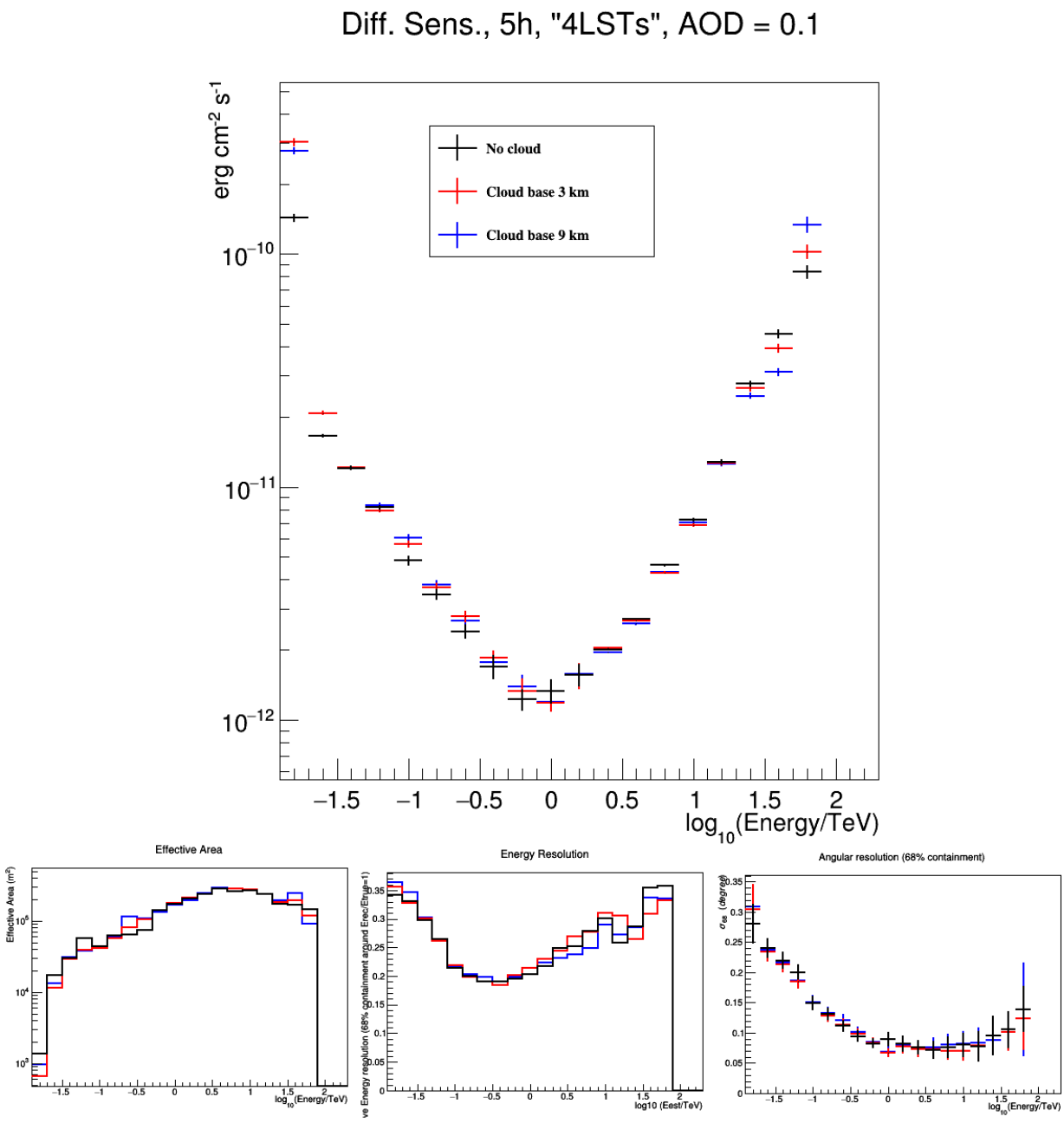

Figure 5.6: ***Top:*** *Differential sensitivity as a function of reconstructed energy, for 4 LSTs configuration, 5 hours long observation and* $AOD = 0.1$. ***Bottom, middle:*** *energy resolution (i.e. 68% containment of the reconstructed incoming photon energy) as a function of reconstructed energy.* ***Bottom, left:*** *effective area as a function of reconstructed energy.* ***Bottom, right:*** *angular resolution as a function of reconstructed energy; average resolution from telescope pointing towards the South and the North at 20 deg zenith are shown. Figures show results for clear atmosphere, and for the atmosphere with clouds at 3 km and 9 km a.g.l.*

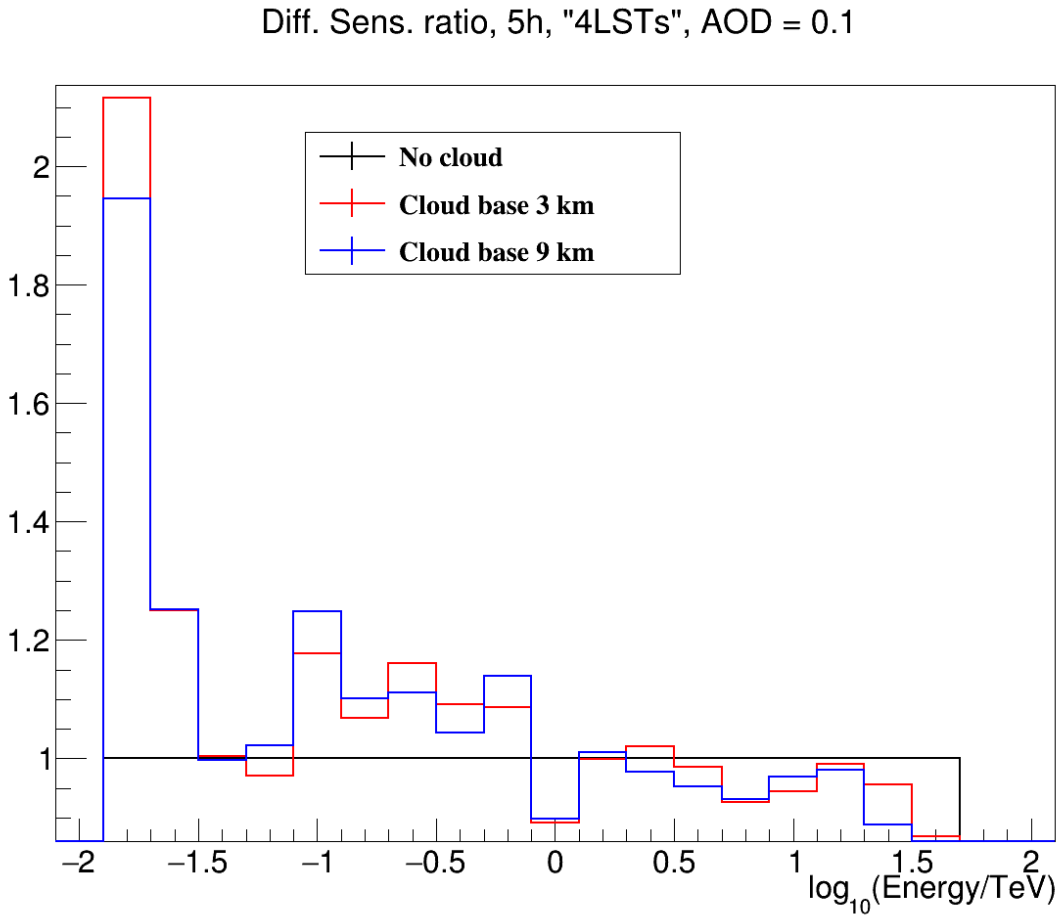

Figure 5.7: *Differential sensitivity ratio as a function of reconstructed energy, for 4 LSTs configuration, 5 hours long observation and* $AOD = 0.1$*. Figure shows results for clear atmosphere, and for the atmosphere with clouds at 3 km and 9 km a.g.l.; smaller ratios mean better sensitivity.*

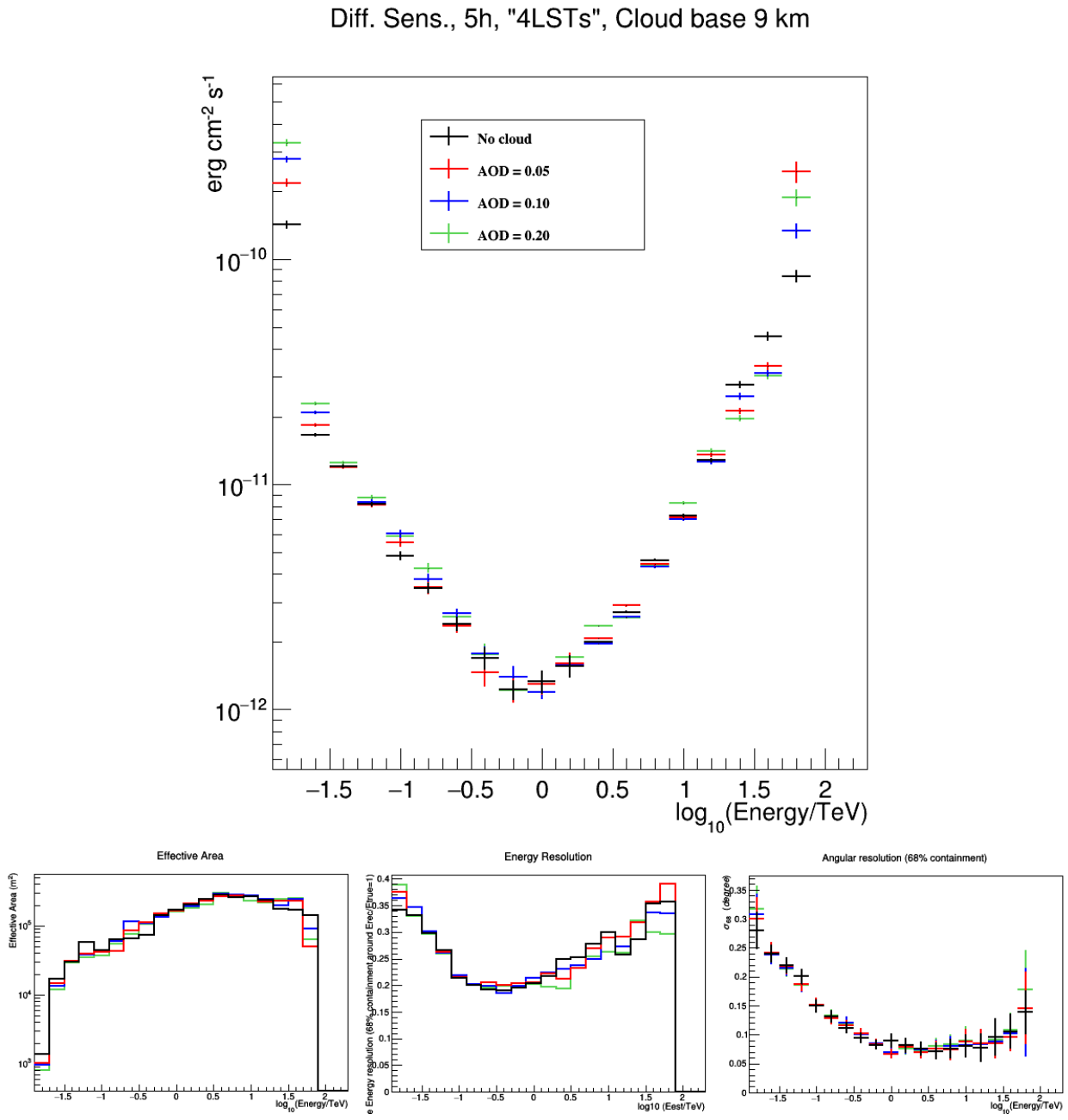

Figure 5.8: ***Top:*** *Differential sensitivity as a function of reconstructed energy, for 4 LSTs configuration, 5 hours long observation, cloud base at 9 km a.g.l.* ***Bottom, middle:*** *energy resolution (i.e. 68% containment of the reconstructed incoming photon energy) as a function of reconstructed energy.* ***Bottom, left:*** *effective area as a function of reconstructed energy.* ***Bottom, right:*** *angular resolution as a function of reconstructed energy; average resolution from telescope pointing towards the South and the North at 20 deg zenith are shown. Figures show results for clear atmosphere, and for the atmosphere with AOD 0.05, 0.1, 0.2.*

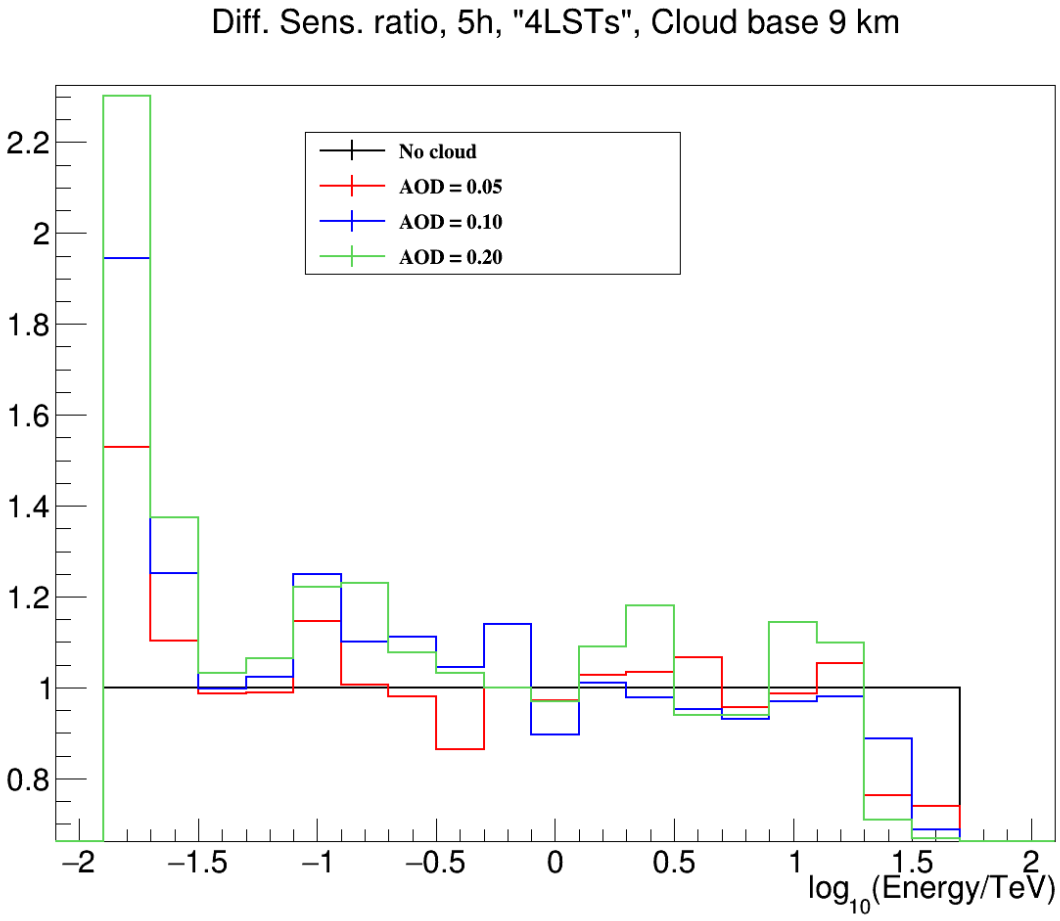

Figure 5.9: *Differential sensitivity ratio as a function of reconstructed energy, for 4 LSTs configuration, 5 hours long observation, cloud base at 9 km a.g.l. Figure shows results for clear atmosphere, and for the atmosphere with AOD 0.05, 0.1, 0.2; smaller ratios mean better sensitivity.*

Summary

This thesis deals with examining the influence of cloud altitude and optical depth on CTA-N performance. Cherenkov radiation is produced in the atmosphere due to the interaction of cosmic gamma-rays with particles present in the atmosphere. On its path to the telescope, Cherenkov radiation can be attenuated, both due to absorption and scattering.

The greatest influence on the attenuation of Cherenkov radiation in the atmosphere has Mie scattering by clouds. Low clouds are formed at altitudes corresponding to the altitude at which telescopes on La Palma are placed. They can be treated as a fog, and during foggy weather, observations are not performed anyway. Thus, low clouds are not simulated. High clouds are located at altitudes above the average altitudes at which Cherenkov radiation is produced, which is why they are not included in the simulations. Only middle clouds called altostratus can have a greater influence on the attenuation of Cherenkov radiation. It is well known that by applying appropriate corrections we can prolongate telescope duty cycle. In order to achieve that, we need to examine the influence of certain clouds of different characteristics on the Cherenkov radiation and telescope response.

We used the MODTRAN software package to simulate transmittance for the atmosphere with clouds. MODTRAN output is a table of transmittances vs. wavelength vs. altitude. Our own Python code is used to transform transmittances into AOD. Models produced by MODTRAN were used as input files for the Monte Carlo simulation with `sim_telarray`. Graphical representations of AOD difference vs. altitude are used as a check-plots in order to ensure that the simulated data is real data for the atmosphere with that particular cloud. The Monte Carlo simulation results are also graphically presented. The differential sensitivity, the effective collection area, the energy resolution, and the angular resolution as a function of reconstructed energy are shown. The results show that the effects of clouds are visible at low energies (even with low statistics), close to the threshold energy.

Obviously, moderate cloudiness does not prevent observations but changes information about the cosmic gamma-rays. Therefore, it is important to understand

and model the influence of different types of clouds (with different densities and at different altitudes) on observations so that we can subsequently correct the data, but also determine which types of objects can be observed at different atmospheric conditions. Knowing the conditions in which corrections can be applied and developing models for particular cases, adaptive scheduling observations become possible.

Since on La Palma about 30% of the observation time affected with transparent high clouds, it is important to use that time, keeping in mind how valuable and important it is. To understand and examine the clouds, and for correction of data, LIDARs, FRAMs (large FOV optical telescopes) and atmospheric modeling software can be used. Instruments which can be used for adaptive scheduling are All-Sky-Camera (ASC) (map of sky cloud coverage) and ceilometer (1064 nm, measurements of cloud height).

The results of this paper are the preliminary results presented at recent conferences (see ref. [10] and [22]). The study is still in progress: in order to give final conclusions about the influence of clouds on the telescope response, simulations with better statistics are being performed by the supercomputer "Bura" at the University of Rijeka.

Bibliography

[1] ACHARYA, B. S. et al. (2013). Introducing the CTA concept. *Astroparticle Physics*. **43:** 3-18.

[2] BIGONGIARI, C. (2016). The Cherenkov Telescope Array. *Nuclear Physics B Proceedings Supplement*. **00:** 1-8.

[3] ALIU, E. et al. (2008). Improving the performance of the single-dish Cherenkov telescope MAGIC through the use of signal timing. *Astroparticle Physics*. **30:** 293-305. (arXiv:0810.3568)

[4] BARRAL, A. F. (2017). *Extreme particle acceleration in microquasar jets and pulsar wind nebulae with the MAGIC telescopes, doctoral dissertation*. Barcelona: Departament de Fısica, Universitat Autonoma de Barcelona.

[5] BARRY, R. G., CHORLEY, R. J. (2003). *Atmosphere, Weather and Climate, 8th edition*. London: Routledge.

[6] BERK, A. et. al. *MODTRAN6: a major upgrade of the MODTRAN radiative transfer code*, Proc. SPIE 9088, Algorithms and Technologies for Multispectral, Hyperspectral, and Ultraspectral Imagery XX, 90880H, 13 June 2014.

[7] BERNLÖHR, K. (2001). *CORSIKA and sim_telarray – Simulation of the imaging atmospheric Cherenkov technique*, `https://www.mpi-hd.mpg.de/hfm/~bernlohr/sim_telarray/Documentation/sim_hessarray.pdf`

[8] BERNLÖHR, K. et al. (2013). Monte Carlo design studies for the Cherenkov Telescope Array. *Astroparticle Physics*. **43:** 171-188.

[9] DEGRANGE, B., FONTAINE, G. (2015). Introduction to high-energy gamma-ray astronomy. *C. R. Physique*. **16:** 587-599. (arXiv:1604.05488)

[10] DOMINIS PRESTER, D., GAUG, M., HRUPEC, D., MAIER, G., MANAGANARO, M., MIĆANOVIĆ, S., TERZIĆ, T. *Simulations of clouds above CTA-N*. CTA General Meeting, Berlin, Germany, 24 September 2018.

[11] FUNK, S. et. al. (2013). Comparison of Fermi-LAT and CTA in the region between 10-100 GeV. *Astroparticle Physics*. **43:** 348-355.

[12] GAUG, M. et al. (2017). *Proposal for the gamma-ray simulation campaign for the CTA-N*, ver. 0.1.

[13] HASSAN, T. et al. (2017). Monte Carlo Performance Studies for the Site Selection of the Cherenkov Telescope Array. *Astroparticle Physics*. **93:** 76-85.

[14] HRUPEC, D. (2008). *Extragalactic sources of rapidly variable high energy gamma radiation, doctoral thesis*. Zagreb: Department of Physics, Faculty of Science, University of Zagreb.

[15] KOKHANOVSKY, A. (2009). Optical properties of terrestrial cloud. *Earth-Science Reviews*. **64:** 189-241.

[16] LI, T.-P., MA, Y.-Q. (1983). Analysis methods for results in gamma-ray astronomy. *Astrophysical Journal*.**272:** 317-324.

[17] LIOU, K. N. (2010). *An Introduction to Atmospheric Radiation, Second Edition*. California: Academic Press.

[18] LONGAIR, M. S. (2011). *High Energy Astrophysics*. New York: Cambridge University Press.

[19] MAIER, G. et al. (2017). Performance of the Cherenkov Telescope Array. *35th International Cosmic Ray Conference (ICRC 2017)*.

[20] MARINKOV, L. (2010). *Osnovi nuklearne fizike*. Novi Sad: Departman za fiziku, Prirodno matematički fakultet, Univerzitet u Novom Sadu.

[21] MAXWELL, J. C. (1865). A dynamical theory of the electromagnetic field. *Philosophical Transactions of the Royal Society of London*. **155:** 459–512. (`http://rstl.royalsocietypublishing.org/content/155/459`)

[22] MIĆANOVIĆ, S., DOMINIS PRESTER, D., GAUG, M., HRUPEC, D., MAIER, G., MANAGANARO, M., TERZIĆ, T. *Influence of cloud altitude and optical depth on CTA-N performance*. AtmoHEAD 2018, Capri, Italy, 24 September 2018.

[23] MUXLOW, T.W.B. et al. (2007). Starburst galaxies. *8th European VLBI Network Symposium*. **036**.

[24] PALATIELLO, M. (2015). *The Cosmic-ray Electron Spectrum Measured with the MAGIC Telescopes, doctoral dissertation*. Udine: Università degli Studi di Udine, Dipartimentio di Chimica, Fisica e Amibente.

[25] PETRIČEVIĆ, M. (2016). *Optimizacija niza Čerenkovljevih teleskopa (CTA) pomoću Monte Carlo simulacija*, https://www.pmf.unizg.hr/_download/repository/sem2015/semPetricevic.pdf.

[26] WALLACE, J. M., HOBBS, P. V. (2006). *Atmospheric Science, An Introductory Survey*. USA: Academic Press.

[27] Cherenkov Telescope Array visualization, http://cdn.eso.org/images/screen/ann14030a.jpg

[28] Official Cherenkov Telescope Array website, https://www.cta-observatory.org/

[29] MAGIC telescope, https://goo.gl/Tg3Vgu

[30] Electromagnetic wave, https://cdn.miniphysics.com/wp-content/uploads/2015/09/EM-Plane-Waves.png

[31] Nolan, P. *Fog, Clouds, and Precipitation*, https://www.farmingdale.edu/faculty/peter-nolan/pdf/Ch05PhysAtms.pdf

[32] Extensive air showers, https://en.wikipedia.org/wiki/Particle_shower

[33] Air showers, https://en.wikipedia.org/wiki/Air_shower_(physics)

[34] COSMOS - The SAO Encyclopedia of Astronomy, http://astronomy.swin.edu.au/cosmos/

[35] Visualisation of clouds classification, https://goo.gl/rFRwLf

[36] Some writtings about lapse rates and clouds, http://web.gccaz.edu/~lnewman/gph111/topic_units/moisture/moisture_stabil_prec/moisture_stabil_prec2.html

[37] Cosmic ray spectrum, https://www.physics.utah.edu/~whanlon/spectrum1.png

[38] About H. Hertz discovery, https://www.famousscientists.org/heinrich-hertz/

[39] Environmental lapse rate, https://www.encyclopedia.com/earth-and-environment/ecology-and-environmentalism/environmental-studies/environmental-lapse-rate

[40] Diehl, L. *Gamma-Ray Production and Absorption Processes*, http://www.mpe.mpg.de/~rod/papers/Universe_2_Processes.pdf

[41] The Online Meteorology Guide, http://ww2010.atmos.uiuc.edu/(Gh)/guides/mtr/home.rxml

[42] Cloud effective radius definition, https://web.archive.org/web/20090724155507/http://disc.sci.gsfc.nasa.gov/PIP/shtml/cloud_effective_radius.shtml

[43] Cherenkov light visualization, https://www.isdc.unige.ch/cta/images/outreach/CherenkovLight.jpg

[44] Some informations about INTEGRAL, https://heasarc.gsfc.nasa.gov/docs/integral/integral.html

[45] Some informations about VERITAS, https://goo.gl/m7zPp4

[46] Some informations about H.E.S.S., https://goo.gl/zbDRoa

[47] Some informations about FERMI, https://goo.gl/ZoA6F7

[48] Some informations about INTEGRAL, https://goo.gl/yZPZrs

[49] MODTRAN offical website, http://modtran.spectral.com/modtran_index

The last access to websites mentioned above was on 10th November 2018.

List of used Codes

Listing 5.1: *Transmittance to AOD transformation Python code.*

```
import numpy as np
import os, glob
import sys
from pathlib import Path

if len(sys.argv) != 3:
  quit()

c = str(sys.argv[1])
n = str(sys.argv[2])

ModtranOutputFileName = "./ext_modtran_output_"+c+"_"+n+".M5"
SimTelArrayInputFileName = "./atm_trans_"+c+"_"+n+".dat"
HeaderFileName = "./header_"+n+".txt"

p = Path(ModtranOutputFileName)
if not(p.is_file()):
  print("input file %s doesn't exist" %ModtranOutputFileName)
  quit()

p = Path(HeaderFileName)
if not(p.is_file()):
  print("header file %s doesn't exist" %HeaderFileName)
  quit()

print("atmosphere %s" %c)
print("simulation %s" %n)
print("input file %s" %ModtranOutputFileName)
print("output file %s" %SimTelArrayInputFileName)

ModtranOutputData = open(ModtranOutputFileName, 'r')
SimTelArrayInputData = open(SimTelArrayInputFileName, 'w')

ModtranOutputLoaded = np.loadtxt(ModtranOutputData)
```

```
35
36 s=0.0
37 v=99999.00
38 wavelengths=len(ModtranOutputLoaded[:,0])
39 altitudes=len(ModtranOutputLoaded[0,:])
40 for i in range(wavelengths):
41   SimTelArrayInputData.write('%i'%(ModtranOutputLoaded[i,0]))
42   for j in range(1,altitudes):
43     for k in range(1,j+1):
44       s+=-np.log(ModtranOutputLoaded[i,k])
45     if s<=12.0:
46       SimTelArrayInputData.write('%.6f'%(s))
47     else:
48       SimTelArrayInputData.write('%.2f'%(v))
49     s=0.0
50   SimTelArrayInputData.write('\n')
51 ModtranOutputData.close()
52 SimTelArrayInputData.close()
53
54 ModtranOutputFileName = ModtranOutputFileName[2:]
55 SimTelArrayInputFileName = SimTelArrayInputFileName[2:]
56 HeaderFileName = HeaderFileName[2:]
57 TemporaryFileName = "tempo.dat"
58
59 with open(TemporaryFileName, 'w') as outfile:
60    for fname in [HeaderFileName,SimTelArrayInputFileName]:
61         with open(fname,) as infile:
62             outfile.write(infile.read())
63
64 os.remove(SimTelArrayInputFileName)
65 os.rename(TemporaryFileName,SimTelArrayInputFileName)
```

Listing 5.2: *AOD difference - altitude graphical representation Python code.*

```
1
2 import numpy as np
3 import matplotlib.pyplot as plt
4 import sys
5 from pathlib import Path
6
7 simSET = 1 # PLEASE, SET IT MANUALLY
8
9 if simSET == 1:
10   totalAOD = 0.05
11 if simSET == 2:
12   totalAOD = 0.1
```

```
13 if simSET == 3:
14   totalAOD = 0.2
15 if simSET == 4:
16   totalAOD = 0.3
17 if simSET == 5:
18   totalAOD = 0.5
19 if simSET == 6:
20   totalAOD = 0.7
21
22
23 if len(sys.argv) != 2:
24   quit()
25
26 n = str(sys.argv[1])
27
28 cloudFileName = "./atm_trans_CLOUD_"+n+".dat"
29 clearFileName = "./atm_trans_CLEAR_"+n+".dat"
30 figureFileNAme = "cloud"+n+".pdf"
31
32 p = Path(cloudFileName)
33 if not(p.is_file()):
34   print("input file %s doesn't exist" %cloudFileName)
35   quit()
36
37 p = Path(clearFileName)
38 if not(p.is_file()):
39   print("input file %s doesn't exist" %clearFileName)
40   quit()
41
42 print("set %d" %simSET)
43 print("simulation %s" %n)
44 print("clear input file %s" %clearFileName)
45 print("cloud input file %s" %cloudFileName)
46
47 fileDATcloud = open(cloudFileName,'r')
48 for i in range(15):
49   line = fileDATcloud.readline()
50   if i==14:
51     DATcloudALT = line
52 DATcloudALT = DATcloudALT[17:]
53 cloudALT = DATcloudALT.split()
54 cloudA = np.array(cloudALT)
55 altitudeCLOUD = np.array([float(i) for i in cloudA])
56 DATcloud = np.loadtxt(fileDATcloud)
57
```

```
fileDATclear = open(clearFileName,'r')
for i in range(15):
  line = fileDATclear.readline()
  if i==14:
    DATclearALT = line
DATclearALT = DATclearALT[17:]
clearALT = DATclearALT.split()
clearA = np.array(clearALT)
altitudeCLEAR = np.array([float(i) for i in clearA])
DATclear = np.loadtxt(fileDATclear)

if not(altitudeCLEAR.all()==altitudeCLOUD.all()):
  print("headers are different")
  quit()

altitude = altitudeCLEAR
wavelengths=len(DATclear[:,0])
altitudes=len(DATclear[0,:])

for i in range(wavelengths):
  if DATcloud[i,:][0] == 550.0:
    cloud = DATcloud[i,1:]

for i in range(wavelengths):
  if DATclear[i,:][0] == 550.0:
    clear = DATclear[i,1:]

deltaOD = cloud - clear
n = int(n)

if (n==15 or n==21 or n==27 or n==33 or n==39 or n==45):
   height = 5.2

if (n==16 or n==22 or n==28 or n==34 or n==40 or n==46):
   height = 7.2

if (n==17 or n==23 or n==29 or n==35 or n==41 or n==47):
   height = 9.2

if (n==18 or n==24 or n==30 or n==36 or n==42 or n==48):
   height = 11.2

if (n==19 or n==25 or n==31 or n==37 or n==43 or n==49):
   height = 13.2

```

```
103 if (n==20 or n==26 or n==31 or n==38 or n==44 or n==50):
104     height = 15.2
105 
106 
107 plt.plot(altitude, deltaOD)
108 plt.axvline(height, c='red',ls='--')
109 plt.axvline(height+1.0, c='red',ls='--')
110 plt.axhline(totalAOD, c='green',ls='--',lw=4)
111 plt.xlabel('Altitude (km)',fontsize=14)
112 plt.ylabel('AOD difference',fontsize=14)
113 plt.title('set %d: CLOUD %d vs CLEAR atmosphere' %(simSET,n))
114 plt.grid(True)
115 plt.xlim(0.0, height+5.0)
116 plt.savefig(figureFileNAme)
117 plt.show()
```

List of frequently used Acronyms

BH	—	**B**lack **H**ole
CORSIKA	—	**CO**smic**R**ay **S**Imulations for **KA**scade
CR	—	**C**osmic **R**ay
CTA	—	**C**herenkov **T**elescope **A**rray
CTA-N	—	**C**herenkov **T**elescope **A**rray - **N**orth
CTA-S	—	**C**herenkov **T**elescope **A**rray - **S**outh
DALR	—	**D**ry **A**diabatic **L**apse **R**ate
EAS	—	**E**xtensive **A**ir **S**hower
ELR	—	**E**nvironmental **L**apse **R**ate
EHE	—	**E**xtreme **H**igh-**E**nergy
EMR	—	**E**lectro**m**agnetic **R**adiation
GRB	—	**G**amma-**R**ay **B**urst
HE	—	**H**igh-**E**nergy
IACT	—	**I**maging **A**tmospheric **C**herenkov **T**elescope
IR	—	**I**nfra**r**ed
LE	—	**L**ow-**E**nergy
LST	—	**L**arge-**S**ized **T**elescope
MAGIC	—	**M**ajor **A**tmospheric **G**ama-Ray **I**maging **C**herenkov
MC	—	**M**onte **C**arlo
MODTRAN	—	**MOD**erate spectral resolution atmospheric **TRAN**smittance algorithm and computer model
MST	—	**M**edium-**S**ized **T**elescope
MW	—	**M**ic**r**o**w**ave
SALR	—	**S**aturated **A**diabatic **L**apse **R**ate
SST	—	**S**mall-**S**ized **T**elescope
SN	—	**S**uper**n**ova
SNR	—	**S**uper**n**ova **R**emnant
UHE	—	**U**ltra **H**igh-**E**nergy
VHE	—	**V**ery **H**igh-**E**nergy

Biography

Mario Pecimotika was born on February 28, 1995, in Virovitica, Croatia. On September 15, 2016, he graduated from the Department of Physics, J. J. Strossmayer University of Osijek with the thesis title *Razvoj ranog svemira* (*The evolution of the early universe*) and received bachelor's degree.

From November 2016 to April 2017 he volunteered at the Elementary School "Antunovac", Antunovac as part of the project *Pomoć u učenju dostupna je i meni* (*The learning support is available to me*) organized by the Volunteer Center in Osijek.

He did his professional training at the Department of Physics, the Faculty of Sciences at the University of Novi Sad, Serbia from 23 June 2017 to 15 July 2017, in the field of gamma spectroscopy.

He is a member of Croatian Physical Society since 2014. He participated at the 10th Scientific Meeting of Croatian Physical Society held from 11th to 13th October 2017 in Baška, Croatia and at the 11th Scientific Meeting of Croatian Physical Society held from 3rd to 5th October 2018 in Beli Manastir, Croatia.

He received Rector's Award for academic year 2016/2017.

Index